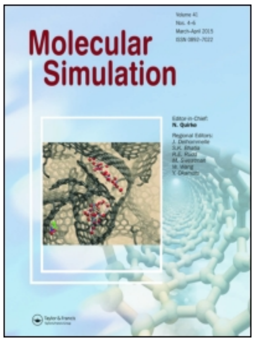

Molecular Simulation

ISSN: 0892-7022 (Print) 1029-0435 (Online) Journal homepage: http://www.tandfonline.com/loi/gmos20

Molecular dynamics simulations reveal how characteristics of surface and permeant affect permeation events at the surface of soft matter

Priyanka Oroskar, Cynthia J. Jameson & Sohail Murad

To cite this article: Priyanka Oroskar, Cynthia J. Jameson & Sohail Murad (2017) Molecular dynamics simulations reveal how characteristics of surface and permeant affect permeation events at the surface of soft matter, Molecular Simulation, 43:5-6, 439-466, DOI: 10.1080/08927022.2016.1268259

To link to this article: http://dx.doi.org/10.1080/08927022.2016.1268259

MOLECULAR SIMULATION, 2017
VOL. 43, NOS. 5–6, 439–466
http://dx.doi.org/10.1080/08927022.2016.1268259

SURFACE CHEMISTRY

Molecular dynamics simulations reveal how characteristics of surface and permeant affect permeation events at the surface of soft matter

Priyanka Oroskar[a], Cynthia J. Jameson[b] and Sohail Murad[c]

[a]Department of Chemical Engineering, University of Illinois at Chicago, Chicago, IL, USA; [b]Department of Chemistry, University of Illinois at Chicago, Chicago, IL, USA; [c]Department of Chemical Engineering, Illinois Institute of Technology, Chicago, IL, USA

ABSTRACT

Molecular dynamics simulations are particularly useful in providing details that permit understanding of phenomena occurring at surfaces, phenomena characterised by surface-sensitive experimental methods yielding average properties. The methods and examples that we consider here reveal how the characteristics of the surface and the permeant affect permeation events at the surface of soft matter, in particular, lipid bilayers. We choose permeation of lipid membranes as our example of the ability of molecular dynamics simulations to provide molecular-level mechanisms that are otherwise not available via other means. Molecular permeation through lipid membranes is a fundamental biological process that is important for small molecules such as therapeutics as well as nanoparticles that have become important modes of drug delivery. We describe methods applicable to such large systems and use examples where the permeants are uncharged particles: small molecules (Xe, O_2, CO_2), bare gold nanocrystals, gold-core nanoparticles with hydrophobic ligands (alkane thiols of various lengths) and gold-core nanoparticles with hydrophilic ligands (methyl-terminated polyethylene glycol of various lengths). In each example, we have previously validated our findings by comparisons with experimental data, using such information as is available from X-ray diffraction, electron paramagnetic resonance, nuclear magnetic resonance, atomic force microscopy, various imaging methods, diffusion measurements, dynamic light scattering. In addition to spherical core nanoparticles, we also examine the characteristic permeation mechanisms of gold nanorods with polyethylene glycol ligands, where the aspect ratio different from 1 makes the permeation event dependent on the angle of the rod axis relative to the membrane surface. This review examines the phenomena associated with the interaction of various permeants with the lipid bilayer that serves as our model membrane. We consider adsorption at the interface, the permeant within the top lipid leaflet, in the middle of the membrane within the lipid tail region, within the bottom lipid leaflet and finally exiting the membrane on the way to recovery, for various permeants: gas molecules, bare gold nanocrystal, gold nanoparticles with alkane thiol ligands, PEGylated gold nanoparticles and PEGylated gold nanorods. We observe formation of a water pore, occasional transport of ions, lipid flip-flops, lipid displacement from the membrane, and rotational behaviour of PEGylated nanorods during the permeation process. These events differ depending on the chemical nature (hydrophobic or hydrophilic) of the ligands, their length, the coverage density on the gold surface and the aspect ratio of the gold core. Direct comparisons across the board are possible by using identical interaction models (MARTINI coarse grain), molecular dynamics methods, simulation set-ups and analyses of MD results, thereby permitting generalisations to be made about mechanisms for the various events and how they are affected by these factors.

ARTICLE HISTORY
Received 7 September 2016
Accepted 28 November 2016

KEYWORDS
Coarse-grained molecular dynamics; lipid membrane; permeation; PEGylated gold nanoparticles; nanorods

1. Introduction

Molecular permeation through lipid membranes is a fundamental biological process that is important for small neutral molecules and drug molecules. An early discussion of permeation of membranes by molecules considered Eyring's Absolute Rate Theory as a theoretical framework [1]. The theory regards the movement of molecules within membranes as a series of successive jumps from one equilibrium position to the next and requires the free energy profile that connects the equilibrium positions. Another approach proposes a diffusion mechanism [2] analogous to the so-called free volume theory of diffusion within polymers [3]. In this theory, it is assumed that transient 'holes' or pockets of free volume are opened up by thermal fluctuations that serve as the passage for diffusing molecules. Yet another proposal is that certain types of mobile structural defects, so-called kinks, which result from conformational changes in the hydrocarbon chains of a membrane, would produce small mobile pockets of free volume of different sizes. A molecule present in the aqueous phase adjacent to the membrane may jump into the free volume of a kink at the membrane surface and may then diffuse across the membrane together with the mobile kink, in a 'hitch-hiking' process [4]. While any of these early proposed

CONTACT Sohail Murad ✉ murad@iit.edu

'molecular' mechanisms are plausible in that thermal fluctuations do occur in the positions of the atoms and groups of atoms in the lipids constituting a membrane, transient holes of free volumes do randomly occur as the groups of atoms undergo thermal motion, and kinks may indeed form in hydrocarbon chains that constitute the tails of the lipids, each does not by itself constitute the unique type of molecular event that makes it possible for a molecule to move from one side of the membrane to the other.

We use a lipid bilayer membrane as an interesting and relevant model for a soft matter surface. We use molecular dynamics simulations to study the movements of atoms and groups of atoms of the simulations system, explicitly including solvent molecules, biologically essential molecules such as O_2, drug molecules, ions, lipids of the bilayer membrane, nanoparticles, and ligands on nanoparticle cores, and we can follow, over the course of a molecular dynamics trajectory, the passage of a molecule or a nanoparticle across a lipid bilayer without the presence of a transmembrane protein. In these molecular simulations, we can carry out 'what-if' computer experiments to determine the factors that affect the permeation events at the surface of soft matter. In particular, we can determine how the membrane composition and dynamics and the morphologies of the membrane and the permeating entity can affect transport across the membrane. At the same time, we can also map out the free energy profile for movement of these permeating entities from one side of the membrane to the other by calculating the potential of mean force. We limit our discussion to examples using model symmetric membranes of a single composition, and permeating entities such as water, ions, gas molecules, nanocrystals and functionalised nanocrystals with ligands of various chemical composition and lengths, although the same methods may be applied also to asymmetric membranes of mixed composition and to nanoparticles constituted of polymer cores and dendritic or bio-conjugated ligands, with or without entrained drug molecules. We use molecular simulations in order to provide information that would be useful for designing nanoparticles for a wide range of biological and engineering applications. The permeation of water across lipid membranes is of paramount importance in biological and technological processes. The membrane conformation is found to play a critical function in water permeation, regardless of the type of lipid. The fluctuations in the potential energy are found to have a significant, if not the exclusive, role in the transportation of water across lipid membranes [5]. Eliciting this type of dynamic information that is crucial to the understanding of the driving force for such an energetically unfavorable but essential process is only possible through molecular dynamics simulations. Permeation of nanoparticles is accompanied by formation of a transient water pore, the lifetime of which depends on many factors that can be investigated by computer experiments. Along with formation of a transient water pore, ion transport could occur, again, depending on the lifetime of the water pore. Recovery time for the membrane structure after a nanoparticle permeation event also depends on various factors, such as size, shape, chemical nature of ligands grafted on its surface, and surface coverage. Some nanoparticles have been observed, in simulations, to induce potentially long-lasting effects on the lipid membrane, such as lipid flip flop and displacement of lipids from the membrane. Such events can lead to changes in composition of the leaflets if mixed lipids are used, and thinning of membranes, if displacement of lipids is significant. For hydrophobic particles, the membrane interior may act as a trap instead of a barrier, that is, a particle may be able to cross one leaflet and then be unable to leave the hydrophobic tail region in the centre of the membrane. Moderately hydrophilic and hydrophilic particles, on the other hand, may be adsorbed at the phosphate and choline head region and experience the largest resistance to permeation in the lipid tail region. Discriminating between various particles may depend on the size, shape, functionalisation and ligand-grafting density of nanoparticles. Dynamic details attending the movement of particles of various structure and morphology can be investigated using molecular dynamics, and by judicious choice of systems it is possible to tease out the various factors. Depending on these factors, water and ion permeation may accompany nanoparticle penetration to varying degrees. Also, depending on these factors, events that may accompany particle permeation, flip-flop and displacement of lipid molecules from the membrane itself or entrapment of particles within the membrane, can thereby result in compromising membrane integrity. The results of such computer experiments are crucial to the prediction of how these factors can affect the efficacy of nanoparticle-based systems for the purpose of delivery of drugs or imaging agents.

2. Methodology used

2.1. Coarse-grained force field

Molecular dynamics simulations were carried out for three saturated lipid bilayer systems with different hydrocarbon chain lengths: DCPC (C_8), DMPC (C_{14}) and DPPC (C_{16}). The molecular structures of these are shown in Figure 1 [6].

The MARTINI coarse grained force field is based on a four-to-one mapping, with four heavy atoms represented by one interaction site [7]. Details of this model have been previously published [8]. In summary, the model has four main interaction sites categories: polar (P), nonpolar (N), apolar (C) and charged (Q). Within a category, sub-categories are distinguished by a letter denoting the hydrogen-bonding characteristics (d = donor, a = acceptor, da = both, o = non) or a number showing the degree

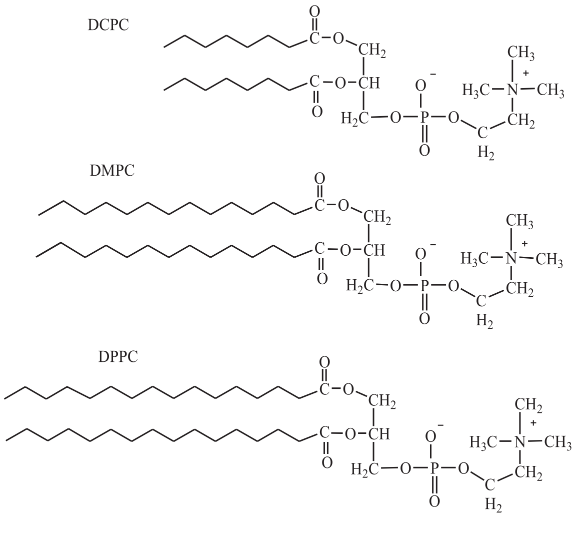

Figure 1. Molecular structures of DCPC (C_8), DMPC (C_{14}) and DPPC (C_{16}) reproduced from Ref. [6].

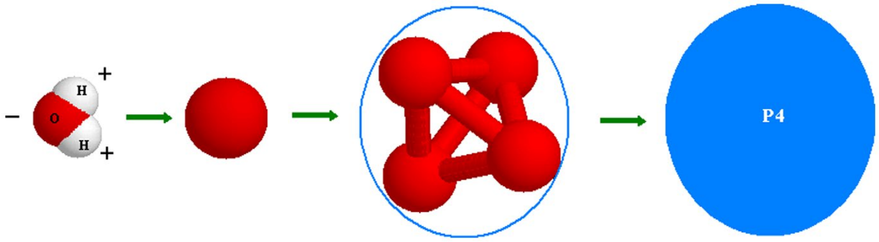

Figure 2. (Colour online) Coarse-grain mapping strategy for water reproduced from Ref [6].

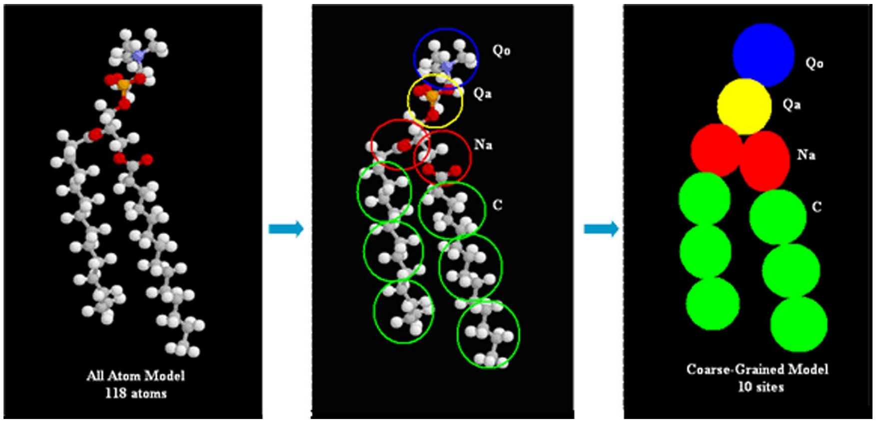

Figure 3. (Colour online) Coarse-grain mapping strategy for a DMPC molecule (blue = choline group, yellow = phospho group, red = glycol group, green = acyl chain); reproduced from Ref [6].

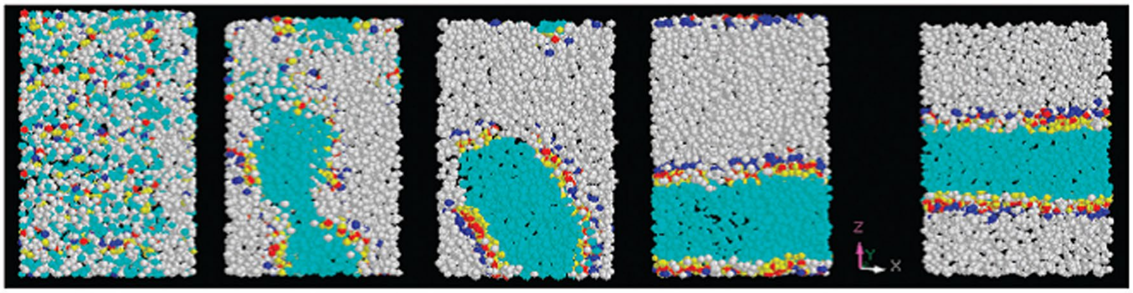

Figure 4. (Colour online) Simulated DPPC lipid membrane self-assemble process (blue = choline group, red = phospho group, yellow = glycol group, cyan = acyl chain, white = water), figure reproduced from Ref. [10].

of polarity (from 1 = lower polarity to 5 = higher polarity). As an example the mapping of a coarse-grained water site (P_4) is shown in Figure 2 [6].

For the lipids, a similar mapping strategy is used, the phospholipid DPPC is modelled with 12 CG sites; DMPC and DCPC have one and two fewer tail beads from each tail, respectively. The mapping of a DMPC molecule is shown in Figure 3 [6].

All site–site interactions i and j at distance r_{ij} are modelled via a Lennard–Jones (LJ) potential:

$$V_{LJ}(r_{ij}) = 4\varepsilon_{ij}\left[\left(\frac{\sigma_{ij}}{r_{ij}}\right)^{12} - \left(\frac{\sigma_{ij}}{r_{ij}}\right)^{6}\right] \tag{1}$$

The energy parameter ε_{ij} values range from ε_{ij} = 5.6 kJ/mol to ε_{ij} = 2.0 kJ/mol for strong polar groups and between polar and apolar groups to capture the hydrophobic effect. The LJ parameter σ = 0.47 nm for all interaction types, except it is set at σ = 0.62 nm that for interactions between charged (Q type) and most apolar types (C1 and C2), to extend the range of repulsion. In addition for charged groups a shifted coloumbic potential function is added in addition to the LJ interaction:

$$U_{\text{elec}} = \frac{q_i q_j}{4\pi\varepsilon_0\varepsilon_r r} \tag{2}$$

In all simulations, the nonbonded interaction has a cut off distance of r_{cut} = 1.2 nm. In addition the LJ potential is shifted at r_{shift} = 0.9 to 1.2 nm and the electrostatic potential is shifted from r_{shift} = 0.0 nm to 1.2 nm using the usual standard shift function [9].

The bonds are modelled by a harmonic potential V_{bond} (R)

$$V_{\text{bond}}(R) = \frac{1}{2}K_{\text{bond}}(R - R_{\text{bond}})^2 \tag{3}$$

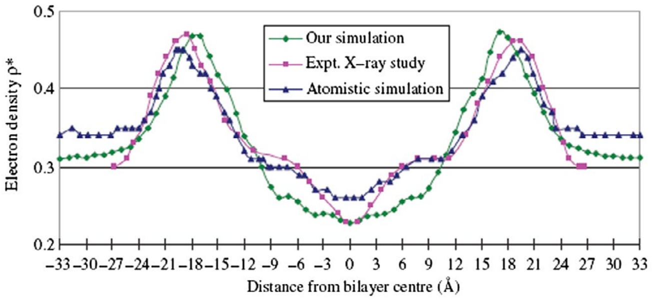

Figure 5. (Colour online) Comparison of simulated electron density (ρ^* in electrons/Å3) for the DPPC bilayer with X-ray experimental measurements and with atomistic simulations Ref. [11], figure reproduced from Ref. [10]

and for bond angles a cosine type harmonic potential $V_{\text{angle}}(\theta)$ is used.

$$V_{\text{angle}}(\theta) = \frac{1}{2}K_{\text{angle}}\{\cos(\theta) - \cos(\theta_0)\}^2 \quad (4)$$

First, we characterised the lipid membrane. We monitored the self-assembly process of the lipid bilayer membrane with 128 DPPC molecules and 2000 water molecules, starting from random orientations and positions. This is a rather stringent test of the model. Snapshots of the configurations for 100 ns are shown in Figure 4 [10], which clearly shows a lipid bilayer membrane forming spontaneously. We performed MD simulations in three saturated lipid bilayer systems with different hydrocarbon chain lengths: dicapryloylphosphatidylcholine (DCPC, C_8), dimyristoylphosphatidylcholine (DMPC, C_{14}) and dipalmitoylphosphatidylcholine (DPPC, C_{16}) [6]. Important quantities characterising a lipid bilayer membrane are the surface area per lipid and the thickness of the membrane. The area per lipid for the self-assembled DPPC at 323 K (50°C) was found to be 68 Å^2 [10], which agrees well with the experimental measurements which lie between 57 and 71 Å^2 [11]. The average distance between phosphate groups is 3.7 nm which is in close agreement with the experimental value of 3.85 nm [11].

If we assign electrons associated with each group of atoms, we can compare the electron density from the simulations with experimental values [11]. Although this comparison of probability profiles is not accurate due to the coarse graining, this permits a direct comparison with atomistic simulations. Our results in Figure 5 [10] show qualitatively consistent behaviour with the experimental electron density profile from X-ray studies and also mimics reasonably well the atomistic profile.

2.2. Simulation set up for permeation of gases

The gas molecules investigated included xenon, oxygen and carbon dioxide. In the case of xenon and oxygen we chose a central LJ model. For CO_2, because of the importance of the electrostatic interactions, we chose a three centred model with point charges. The potential parameters used for these molecules are listed in Table 1.

For all cross-interactions between gas sites and lipid/water sites, the Lorentz–Berthelot mixing rule was used, although we may in the future used cross parameters to obtain a better description of the interactions [15].

Table 1. Potential parameters of gas molecules studied.

Molecule	Interaction sites	σ(Å)	ε(k)	Q (e)	r_{bond} (Å)
O_2 [12]	Central LJ	3.36	120	0	
Xe [13]	Central LJ	3.9478	228	0	
CO_2 [14]	C	2.757	28.129	0.6512	1.149
	O	3.033	80.507	−0.3256	

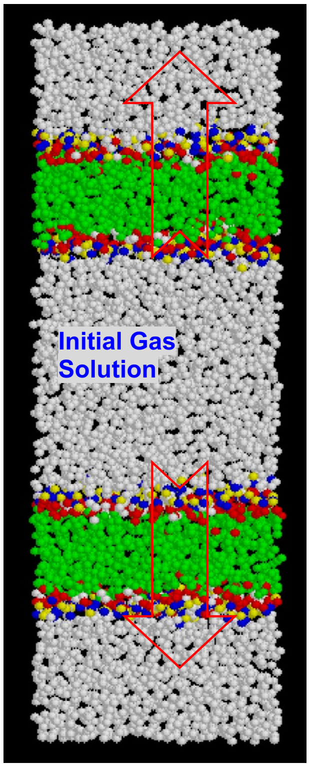

Figure 6. (Colour online) Simulation system for gas permeability measurement (DMPC example), figure reproduced from Ref. [6]. For colour key please see Figure 3.

We propose an approach for examining permeation that closely replicates a real experiment. Previous simulation studies reported often started with gas molecules on both sides of a single lipid layer [16] or else in the inner hydrophobic section of the lipid membrane [17]. Our system consists of two bilayers separated by aqueous phases ('inside' and 'outside') and with gas molecules only in the aqueous middle compartment between the two layers, as shown in Figure 6 [6]. The gas molecules must cross/permeate the membrane to move from the 'inside' to 'outside'. By following changes in the density profile, we were able to measure the diffusion coefficient of a gas through the membrane till equilibrium is reached, the net flux across the bilayer approaches zero.

2.3. Working definition of permeability

Based on the conventional solubility-diffusion model and accounting for the complexity of lipid bilayers, Marrink and Berendsen [18,19] have developed a inhomogeneous solubility-diffusion model. Based on this model, the permeability coefficient P can be calculated by the following equation:

$$\frac{1}{P} = \int_{z_1}^{z_2} R(z)\mathrm{d}z = \int_{z_1}^{z_2} \frac{\exp\{\Delta G(z)/k_B T\}}{D_z(z)}\mathrm{d}z \quad (5)$$

where z_1 and z_2 represent the z coordinates of the two end points of the bulk aqueous phase, $R(z)$ is the local resistance to permeation, $\Delta G(z)$ and $D_z(z)$ are the excess free Gibbs energy and the local diffusion coefficient, respectively, of a small molecule permeating the membrane, while k_B is the Boltzmann constant, and T the temperature.

An alternate approach to the solubility-diffusion mechanism has been proposed by Jansen and Blume [20] based on the transient pore mechanism. This mechanism is based on transport of water molecules largely occurring across a transient pore in the lipid bilayer. The actual mechanism of permeation of small molecules across a lipid bilayer is still not well understood and in addition experimental results are often inconsistent with each other too [21].

To enable direct comparisons with experimental measurements, we introduce a definition of gas permeability as follows [22]:

$$P = \frac{D_{\perp}}{D_{//}} \tag{6}$$

$$\text{Here } D_{\perp} = D_z = \frac{1}{2 \times 1} \lim_{t \to \infty} \frac{\left\langle |r(t) - r(0)|^2 \right\rangle_z}{t} \tag{7}$$

$$\text{and } D_{//} = D_{x+y} = \frac{1}{2 \times 2} \lim_{t \to \infty} \frac{\left\langle |r(t) - r(0)|^2 \right\rangle_{x+y}}{t}$$

If the membrane is completely impermeable, the ratio of $\frac{D_{\perp}}{D_{//}}$ will approach zero. At the other extreme, if the gas molecule can freely permeate the membrane, the ratio will be 1. In most cases the permeability will be between 0 and 1. Our previous work on permeability of ions through membranes, [23] has shown that this definition is qualitatively very comparable with experimental measurements.

2.4. Cycled annealing

Cycled annealing simulation methods are useful in cases where a model system might get stuck in a local minimum and where a global minimum needs to be reached. When model systems are subjected to high temperatures, parameter space is more widely explored for the many degrees of freedom of the system. At lower temperatures, the exploration is restricted and molecules can become trapped in local minimum structures that are artificial when compared to experimental observations. In cycled (or simulated) annealing, a model system is heated to temperatures high enough for molecules to explore the parameter space sufficiently. This is followed by step-wise cooling to the final desired temperature. When the cooling is carried out at a slower rate, the global minimum of the molecular positions and configurations may be reached. Simulated annealing is used in many computational applications including obtaining the structure of functionalised nanoparticles with various ligand types [24] or determining the correct folded structure of a protein [25]. We employed cycled annealing in our work to obtain equilibrium structures for gold nanoparticles with various lengths of attached alkanethiol or PEG ligands.

2.5. Construction of nanoparticles

There is significant interest in gold nanoparticles (AuNP) functionalised for biological and biomedical applications; some examples include bio-imaging, single molecule tracking, drug delivery and diagnostic applications [26–29]. Gold nanoparticles can be engineered to preferentially target tumor cells using appropriately functionalised ligands, which could then be an effective tool for cancer diagnosis and therapy [30]. These applications have motivated our work to employ gold nanoparticles as our model nanoparticles. The structure of the gold nanocrystals (nanoparticle without ligands can be simply obtained by cutting a nearly spherical nanocrystal out of a bulk face-centred-cubic (FCC) structure gold lattice, with a diameter of 2.1 nm. We then attach ligands to the surface of such a 2.1 nm gold nanocrystals using the following procedure: The nanocrystal is placed in the centre of a 12.0 × 12.0 × 12.0 nm^3 simulation cube to which are added butanethiol (ligands) in excess of what would be required to form a compact monolayer. We then followed cycled annealing simulations to condense the ligands onto the surface of the nanocrystal, following the method reported by Luedtke et al. [31] in a similar atomistic investigation. The temperature cycled from 200 to 500 K to allow adsorption, stable binding and desorption of excess ligand molecules. We found the final number of the equilibrated butanethiol chains on the gold core to be 87, resulting in a thiolate surface gold atom coverage of 48.3% (a surface density of 6.28 ligand nm^{-2}), which is within the range of experimental coverage measurements, up to 52–57% for 2.1 nm diameter alkanethiolate gold nanoparticles [32]. As can be seen from Figure 7(a) [33], following the annealing process, the surface sulfur atoms are uniformly distributed on the nanoparticles and the distances between sulfur atoms range from 0.44 to 0.51 nm (Figure 7(b)). To investigate longer ligand lengths, the butanethiol ligands are replaced by R = $(CH_2)_8$ and R = $(CH_2)_{12}$ to form gold nanoparticles with neutral hydrophobic ligands of medium length and longer length, shown in Figure 7(c).

The gold nanoparticles used here (2.1 nm diameter) are smaller than those typically used in biomedical applications. In experimental studies a wide range of sizes of Au nanoparticles have been used for applications such as drug delivery and as imaging agents. Nanoparticles in most studies range from 1 to 100 nm [34]. PEG-coated AuNPs (4 and 100 nm) have been reported to be administered intravenously to mice [35]. Pan et al. have studied the size dependence of cell toxicity of gold nanoparticles that are water soluble with sizes between 0.8 and 15 nm in diameter and concluded that all were most sensitive to gold particles 1.4 nm in size in all four cell lines investigated [36]. Hainfeld [37] used 1.9 nm diameter Au NPs for imaging in mice. We believe, our 2.1 nm nanoparticles, while small, are appropriate for many applications. We do note that gold nanoparticles used for biomedical applications such as gene and drug delivery are usually larger (20–100 nm). This is because they are often conjugated with other biomolecules or drugs and thus these larger sizes are known to permeate cell membranes efficiently using mechanisms such as endocytosis, which is not studied in our work.

In our simulations, we followed the following atomistic to coarse-grained mapping strategy: the gold and sulfur atoms are mapped 1:1 and assumed rigid/fixed. The residues of alkyl chains

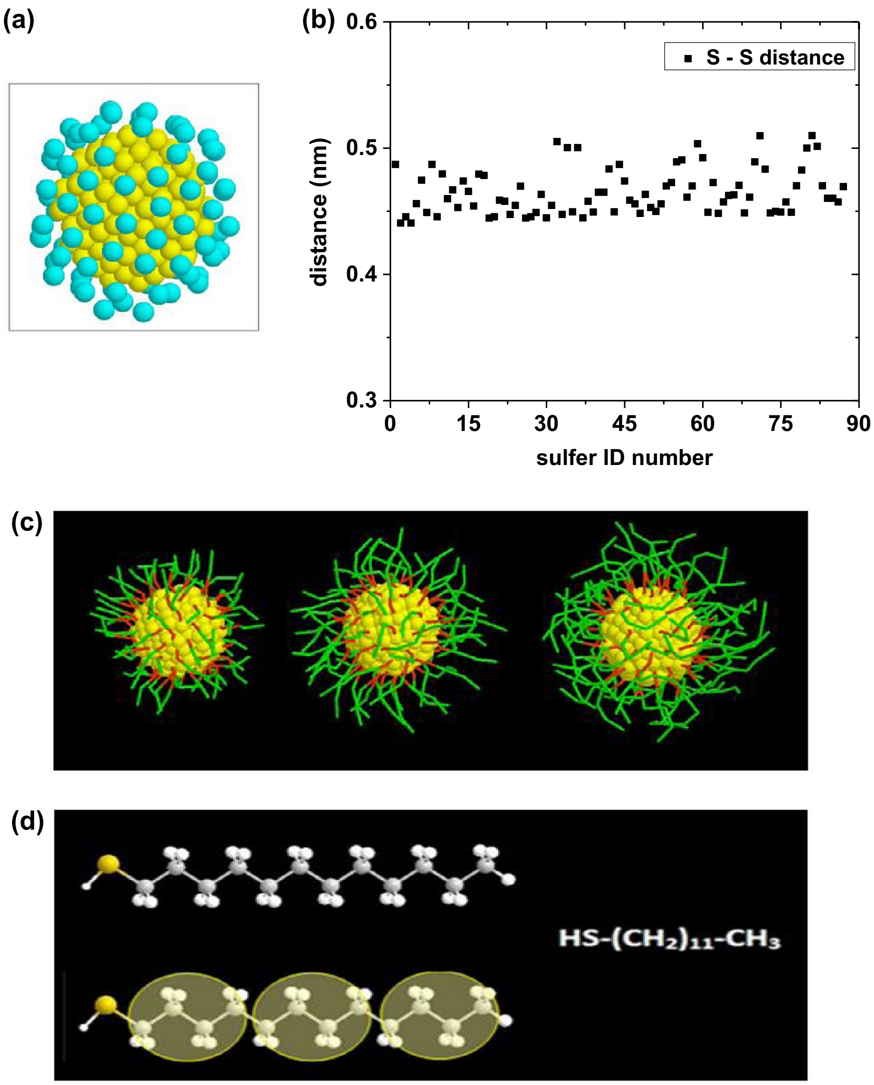

Figure 7. (Colour online) A schematic illustration of the structures of nanoparticles used in simulations. (a) Distribution of surface atoms on the gold core (2.1 nm); (b) The distance between sulfur-sulfur atoms on the surface of the gold core; (c) The structure of the nanoparticles. The residues are replaced by R = $(CH_2)_n$ to form nanoparticles; shown here are structures for $n = 4, 8, 12$ from left to right; (d) The structure of one alkyl residue and the coarse-grained mapping strategy from atomic sites to coarse-grained sites. Figure reproduced from Ref. [33].

Table 2. Nanoparticle force field (R_0 in nm, K_{bond} in kJ mol^{-1} nm^{-2}, Θ_0 in deg, K_{angle} in kJ mol^{-1} rad^{-2})

Non-bond		Bond			Angle		
Interaction site	Type[a]	Connecting block	R_0	K_{bond}	Connecting block	Θ_0	K_{angle}
Au	C5	Au-S	0.445	1250	Au-S-Ligand	180	25
S	N0	S-Ligand	0.445	1250	S-Ligand-Ligand	180	25
Ligand	C1	Ligand-Ligand	0.47	1250	Ligand-Ligand-Ligand	180	25

[a]MARTINI classification.

are 4:1 mapped and flexible (1(d)). The interactions between the gold nanoparticle and lipid molecules is modelled by L–J potential model. A wide range of potential parameters have been used in previous studies for gold atoms; these include all-atom [38–40] or coarse-grain (these include atomistic structures but gold atoms modelled as either C-class [41] or P-class [42] using MARTINI force fields). In our studies we have used MARTINI C5 type interaction sites for gold atoms, N0 type have been used for sulfur atoms and C1 type for alkyl chains. These classes of interaction sites and the corresponding potential parameters have been tested and verified against atomistic simulations by Marrink et al. [17] and we have, in addition, tested them in our simulation studies by comparing with experimental data for lipid membranes [10]. The parameters for non-bonded and bonded interactions for gold nanoparticles are shown in Table 2. As was done previously, for the cross-interactions we used the standard Lorentz–Berthelot mixing rules [15].

For PEGylated nanoparticles we equilibrated a 10.0 × 10.0 × 10.0 nm^3 simulation box of PEG3-SH which resulted in a density of 1053.6 kg/m3 using the NPT ensemble at 400 K (above the glass transition temperature of PEG [43,44] for 5 ns. This agrees well with the value 1048 kg/m^3 from experimental measurement and extrapolation [45]. We then inserted a 3.1 nm diameter gold nanoparticle in this system but now in an NVE ensemble at 400 K for another 5 ns. Once we approached equilibration, we switched to the NPT ensemble once again for the cycled annealing simulation. Many groups have simulated polymer nanocomposites, nanoparticles immersed in polymer melts, where polystyrene or polyethylene oxide polymer melts were doped with spherical nanoparticles or nanorods of various aspect ratios [43,45–48]. Generally, simulations with polymer melts must be carried out with temperatures higher than the glass transition temperature to properly capture the structural properties of the polymer melt, which would otherwise begin to order at lower temperatures [49].

In all of the cycled annealing simulations, the thiol group is the attachment site of the PEGn-SH ligand. We began by heating the system to a high temperature of 1200 K to allow the ligands to explore a variety of stable binding sites on the nanoparticle surface and to favour desorption of excess ligands from the nanoparticle surface. In previous simulations of silica nanoparticles with PEG melts, temperatures of up to 1200 K [50] have been used. During the system cooling stages, we permitted the temperature to drop slowly by 20 K/ns for 5 ns. Once the system had been cooled to the final temperature (323 K for our simulations), we equilibrated the system for over 50 ns.

When constructing PEGn-SH functionalised gold nanoparticles with various ligand lengths, it is not reasonable to assume that coverage is independent of ligand length, since experimentally synthesised PEGylated nanoparticles show that the coverage density of PEG on the nanoparticle surface decreases as the chain length/molecular weight increases [51]. The cycled annealing simulation with short PEG ligands resulted in a PEGylated AuNP with high coverage density. In the case of PEG3-SH ligands, we found that 75 ligands condensed on the nanoparticle surface which translates to a coverage of 2.49 ligands/nm^2. To investigate PEG6-SH AuNP and PEG12-SH AuNP systems, we used our equilibrated PEG3-SH AuNP nanoparticle in solution of PEG3-SH ligands as a starting point for our next simulations to construct PEGylated AuNPs with longer PEG ligands; to construct PEGylated gold nanoparticles with longer ligands, we attached additional beads to the former and attached additional beads to the ligands in the melt. After we equilibrated the new nanoparticle with longer ligands in the solution of its respective melt, we subjected the system to the same cycled annealing procedure. From this, we obtained a PEGylated AuNP with longer PEG ligands that had, in comparison, a lower coverage density. For example, these simulations resulted in a PEG6-SH AuNP with 50 ligands condensed and a PEG12-SH AuNP with 32 ligands condensed, corresponding to a coverage of 1.66 and 1.06 ligands/nm^2, respectively. In separate simulations, we also completed a cycled annealing simulation for a bare gold nanoparticle in an isotropic melt of longer PEG ligands, directly. Using this alternate method, we obtained the same surface coverages for longer length PEGylated AuNP as we obtained using the replacement method. Other groups who have synthesised PEGylated nanoparticles have also reported a range in PEG coverage of 0.2–2.0 ligands/nm^2 [52].

2.6. Nanoparticle permeation

We used an external force in the range of 50–1000 pN to aid the permeation of the nanoparticles in the membrane with velocity in the range 0.35 to 1.4 m/s [33,53] (The nanoparticle permeation velocities we examined here are 0.35, 0.525, 0.7 and 1.4 m/s respectively. The external forces we applied are significantly smaller than the forces for example between two nanoparticles – 0 to 12 nN [54] or nanoparticles and cell membranes – 50 to 1200 pN [55]. The nanoparticle velocities investigated (resulting from the forces applied) are larger than some experimental studies, these are however still several orders of magnitude smaller than the thermal velocities of water, ions and lipid molecules (96.6–334.5 m/s) at the temperature investigated, and an order of magnitude smaller than thermal velocities of nanoparticles (7.5–51.0 m/s). Therefore, we believe our simulations still represent the permeation process realistically, although the process has been facilitated to shorten the permeation time significantly due to computational constraints. This is also demonstrated by the recovery of the lipid layer between two permeation cycles indicating no permanent damage to the membrane at these velocities [6]. Other simulations [56,57] have used similar velocities and their results also appear in reasonable agreement with experiments.

These described methods are generally applicable to many simulation systems; in addition we also have used methods of describing our simulation results in various ways that reveal physical insight provided by MD. The latter methods are described and illustrated in the various examples below.

3. Examples

Examples that we consider here reveal how the characteristics of the surface and the permeant affect permeation events at the surface of soft matter, in particular, lipid bilayers. We choose permeation of lipid membranes as our example of the ability of molecular dynamics simulations to provide molecular-level mechanisms that are otherwise not available via other means because molecular permeation through lipid membranes is a fundamental biological process that is important for small molecules such as therapeutics as well as nanoparticles that have become important modes of drug delivery. We will group our examples in terms of the molecular level events and phenomena that have been ‘observed’ in MD simulations. We will discover how these events and phenomena are affected by various factors, particularly those factors that are characteristic of the intruding particle. All the simulations were performed with the LAMMPS simulation package [58].

3.1. Adsorption of small molecules at the interface and penetration of small molecules through the lipid bilayer

The permeation rate of gas molecules through biomembranes is relatively small. To observe the permeation of gas molecules across the membrane quantitatively would either require large concentration of gas molecules (which is not realistic except under very high pressures which may affect the stability of the biomembrane), or very large systems, or long simulation times. The dynamics in CGMD are faster than that for fully atomistic simulations because the CG interactions are much smoother compared with atomistic interactions. We have used molecular dynamics simulations with the CG MARTINI force field to gain semi-quantitative insights into the gas permeation process through lipid bilayers [6]. We studied low-pressure (below 10 bar) solutions and carried out simulations for 100 ns. Our simulations gave us a relatively reliable qualitative picture of the permeation rates in these systems. Instead of aiming for a complete analysis, we have attempted to gain a basic insight of the mechanism by which the gas molecules permeate lipid membranes.

Our approach for examining permeation closely replicates a real experiment. We designed a system with two bilayers separated by aqueous phases ('inside' and 'outside') and with gas molecules to be introduced into the aqueous middle compartment formed by the two layers, as shown in Figure 6. First, the DPPC–water system is equilibrated; then, eight xenon atom as molecules, since the solubility of xenon in water is rather low. This avoids the situation where the pressure in the middle compartment becomes large and affects the stability of the lipid bilayer membranes. At the onset of the simulation, the gas molecules can therefore only permeate from 'inside' to 'outside'. At 10 ns, the xenon has started to permeate through the lipid bilayer. The xenon density in the compartments outside is low and the xenon atoms are starting to exit the membrane. Between 10 and 100 ns, the xenon continues permeating across the lipid bilayer and finally after 100 ns the system approaches equilibrium, the inside and outside density profiles become almost uniform. We measure the diffusion coefficient of the gas through the membrane until the gas concentration gradient has diminished to nearly zero, which is a sign of equilibrium, and a net flux across the bilayer of zero.

A meaningful comparison with experimental studies is possible with permeability as defined in Equation (6): the ratio of diffusion coefficients in the *z* direction (perpendicular to the membrane surface) to diffusion coefficient in the *xy* plane (parallel). The mean square displacement (MSD) curves for the first 10 ns can be used to calculate the permeability using Equations (6)–(8) [6].

By using this definition of permeability, we can compare our simulation results directly with the experimental results without additional concerns about the conversion of the CG time scales to real time, a well-known problem in CG simulations [59]. For *diffusion constants, the CG model results are 2- to 10-fold larger in comparison with the* atomistic simulations [60]. These problems do not affect our permeability values because we take a ratio.

The permeability of xenon through DPPC membrane at 323 K is found to be 0.334 ± 0.06 and for oxygen it is 0.775 ± 0.11. The value for oxygen can be compared with experiment. Subczynski et al. [61] have reported an experiment to measure permeability of oxygen through a Chinese hamster ovary plasma membrane using spin-labelled stearic acid. Spin labels were synthesised into the hydrocarbon tail of stearic acid at one of three locations: at the end, in the middle, or near the head. A very low concentration of these spin-labelled stearic acid molecules were intercalated within the membrane. By measuring the relaxation time change of the spin labels in the lipid bilayer portion of the membrane, the collision rate of oxygen with the spin labels was estimated and hence profiles of the local oxygen transport parameters across the membrane were obtained. The authors calculated the permeability for O_2 as the ratio of the permeability coefficient across the membrane to the permeability across the water layer, which is comparable with our calculation of permeability. The comparison of our calculated results with their experimental results is shown in Figure 8 [6]. We find that our result at 323 K is qualitatively consistent with their experimental results at three lower temperatures [61]. Since details of the structure for the membranes being studied here are only available at higher temperature (323 K) and phase changes can occur at lower temperatures, simulations at the lower temperatures to compare directly with the experimental data would not be realistic.

We also carried out simulations in which the outer membrane protein A (OmpA) is included, spanning the model membrane [10]. In the OmpA protein, some amino acid sites include charges; the overall OmpA is negatively charged (-3e). For simplicity, we did not include counterions and we employed the known structure for open pore OmpA. One OmpA N-terminal transmembrane protein is represented by 369 CG sites. Water molecules spontaneously fill the OmpA channel. The density profile of water is quite uniform in the middle of the pore, with an average density of water in OmpA channel of 0.027/Å^3. With the OmpA protein channel present, the pathways for the gas molecules are either through the OmpA pore or through the lipid bilayer directly. Over a 100 ns simulation, we monitored the permeation of various gases in OmpA-containing membranes. We observe that in the DPPC membranes as well as in the OmpA channel, the *permeation rate increases as the molecular size decreases*, as expected. However, the rate of increase is much more dramatic in the OmpA channel than the DPPC bilayer which offers a much more tortuous path to the molecules. From Table 3, we can see the effect of the OmpA channel on gas permeability. Here, we compare with gas permeation through pure lipid bilayer [6]. Overall it does not appear that the permeability of small molecules is particularly enhanced by the presence of the OmpA channel, although there is a consistent increase of about 20% in our system with stoichiometry of 1 OmpA/205

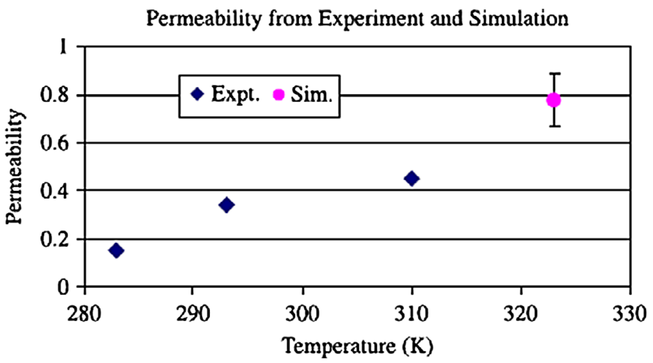

Figure 8. (Colour online) Comparison of permeability of oxygen in biomembrane and our model membrane (Sim.), figure reproduced from Ref. [6], experimental data Ref. [61].

Table 3. Permeability of gas molecules in lipid and OmpA-lipid systems, reproduced from Ref. [10].

Gas	Permeability through DPPC	Permeability through DPPC with OmpA
Xe	0.334 ± 0.06	0.548 ± 0.04
CO_2	0.464 ± 0.07	0.65 ± 0.10
O_2	0.775 ± 0.11	0.714 ± 0.09

Table 4. Comparison of radius of gyration and diffusion coefficient of the CG gold nanoparticles with simulation reports and experimental measurements.

Ligand	Radius of gyration (nm) in hexane			Diffusion coefficient (10^{-6} cm^2/s)		
	Simulation [33]	Simulation [62]	Experiment [63]	Simulation [33]	Simulation [62]	Experiment [63]
$HS\text{-}(CH_2)_7\text{-}CH_3$	0.991			1.310	1.333 ± 0.25	2.6 ± 0.3
$HS\text{-}(CH_2)_{11}\text{-}CH_3$	1.138	1.145 ± 0.004	0.924 ± 0.005	1.073	0.918 ± 0.04	2.3 ± 0.2

lipid (approximately 4 percent of the surface is occupied by the OmpA channel).

For CO_2 an increase is observed, primarily because of the availability of the OmpA channel. For oxygen, the effect is relatively small. Because of its smaller size it can readily permeate both the channel and the membrane. We did not observe any xenon atoms transported through the OmpA channel (Xe is too large); they permeate through the water–lipid interface. We observed the xenon permeability is increased in the OmpA/lipid system. Since all xenon atoms permeate through the lipid membrane via dynamically formed pores at the water–lipid surface, this increase is probably attributable to the change in lipid structure near the protein lipid interface; the incidence of dynamically formed pores is enhanced by having a protein embedded in the membrane. Based on the simulation results, the overall physics of membrane permeation by gases is straightforward and easily understood as a consequence of lateral area fluctuations. In some cases (not Xe) additional permeation occurs through pores of transmembrane proteins embedded in the membrane. These proteins also affect permeation through the lipid bilayer via protein–lipid interactions which change lipid structure near the proteins.

Our studies do not include active transport, where the mechanism of permeation can be much more complicated.

3.2. Characterisation of the ligand-coated nanoparticles

The structure of the ligand-covered nanoparticle can influence the nature of its interactions with the membrane molecules; thus testing its properties against experimental characteristics is crucial. To validate the models used, a wide range of properties of ligand-coated gold nanoparticles were investigated to test the effectiveness of the model we have used for gold nanoparticles. For example, for the alkanethiol-coated nanoparticles, a $10.8 \times 10.8 \times 10.8$ nm^3 simulation system with a nanoparticle placed at the centre in a solvent was examined. In this system we calculate the nanoparticle radius of gyration by allowing each gold nanoparticle to dissolve in a hexane solution at 300 K. Two C1 beads having a 0.47 nm harmonic bond between them represented the CG hexane solvent. This particle-solvent system was allowed to equilibrate for 20 ns with a time step of 10 fs and the radius of gyration was averaged after every 400 ps. Following this, we calculated the nanoparticle diffusion coefficient by inserting a nanoparticle insert into a $CDCl_3$ solution. The overall system was similar to the previous case, except a C4 bead represented the CG $CDCl_3$. The diffusion coefficient is estimated using the long-time slope of the MSDs. The values for nanoparticle radius of gyration and the diffusion coefficient for AuNP nanoparticles with 8- and 12- alkane ligands, are shown in Table 4, [33] and can be seen to be consistent with Lin's previous coarse-grained simulation study [62]. We also observe that our radius of gyration is slightly larger than the experimental measurements, accompanied by a smaller diffusion coefficient in $CDCl_3$ solution compared to the experimental study [63]. These results are internally consistent because a larger gyration radius will induce more friction in the solution, thus having a negative effect on the diffusion. These observations show that our simulations are in reasonable qualitative agreement with available experimental results, which we believe validate the applicability of the coarse-grained model we are using for the ligand-coated gold nanoparticles.

To validate our obtained PEGylated nanoparticles, with coverage densities between 1.0 and 2.5 ligands/nm^2 [64], we compare with experimental data for synthesised PEGylated gold nanoparticles. Many groups [65] reported a range in PEG coverage density of 0.2–2.0 ligands/nm^2 with the exception of Rahme [66] and co-workers who observed a higher grafting density of 3.93 ligands/nm^2. Our PEGylated gold nanoparticles obtained

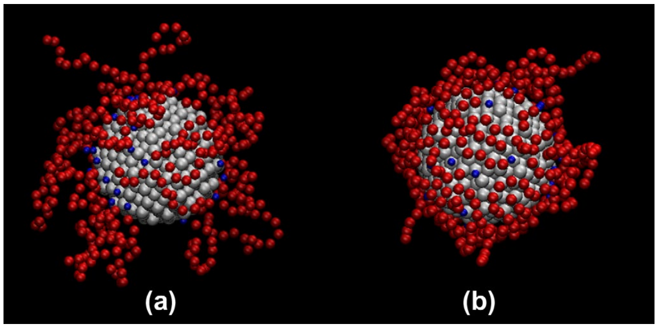

Figure 9. (Colour online) Snapshots of equilibrated PEGylated gold nanoparticle in the (a) melt and (b) in presence of water. The gold nanoparticle core is pictured in white with the sulfur beads (blue) and PEGn ligands (red). For clarity, the solvent molecules are not shown.

Table 5. Characteristic properties of individual PEG chains on PEGylated gold nanoparticle.[a]

PEGylated gold nanoparticle (Coverage = 1.06 ligands/nm^2)	R_g of PEG AuNP (nm)	Avg. Radius of NP (nm)	Avg. V_{ligand} (nm^3)	Avg. R_g of PEG chain (nm)	Avg. R_{ee} of PEG chain (nm)
Equilibrated in PEG melt	1.86 – 1.87	2.97 ± 0.69	2.89 ± 0.04	0.75 ± 0.14	1.79 ± 0.71
Equilibrated in water	1.62 – 1.63	2.35 ± 0.51	1.23 ± 0.04	0.75 ± 0.12	1.56 ± 0.66
Equilibrated in 1.4 mol % NaCl	1.62 – 1.63	2.35 ± 0.39	1.20 ± 0.04	0.73 ± 0.11	1.55 ± 0.56

[a] This table reproduced from Ref. [64].

from simulations have grafting densities comparable to what is observed experimentally.

We equilibrated the PEGylated nanoparticle in water for over 200 ns and obtained characteristics of the structure of the functionalised nanoparticle to compare with the structure obtained in the presence of the polymer melt. We present in Figure 9, typical snapshots of a typical PEGylated gold nanoparticle in presence of the polymer melt after cycled annealing was completed (Figure 9(a)) and the same PEGylated gold nanoparticle in water after 200 ns of equilibration was completed (Figure 9(b)).

Important defining properties of polymers include their average radius of gyration (R_g) and the average end-to-end distance of individual PEG chains ($\langle R_{ee} \rangle$). These characteristics are used to describe the behaviour of the polymer in various solutions such as polymer melts, or other aqueous solutions. We obtained the average radius of the PEGylated nanoparticle, average volume occupied by a condensed PEG ligand, average radius of gyration (R_g) and the average end-to-end distance of individual PEG chains ($\langle R_{ee} \rangle$). We defined the average radius of the functionalised nanoparticle as the mean distance between the centre of the gold core to the terminal bead on the attached chain. The average volume of a grafted chain was obtained by taking the difference in volume of the gold nanoparticle pre- and post-functionalisation with PEG and dividing this by the total number of attached chains. We also examined the behaviour of PEGylated gold nanoparticles in a salt solution to compare to the behaviour of the PEGylated nanoparticle in water in Table 5.

Each value in the table is obtained by averaging configurations of the PEGylated nanoparticle every 100 ps over 1 ns post-equilibration by 200 ns.

From Table 5, it is clear that the radius of gyration, the average radius of the PEGylated nanoparticle, and the average volume per PEG ligand decrease in the presence of water compared to in the polymer melt. The average end-to-end distance of individual PEG chains ($\langle R_{ee} \rangle$) decreases when the nanoparticle is equilibrated in water compared to when it is in the polymer melt, but the average radius of gyration of individual PEG chains does not differ significantly in the melt or in water. The characteristics of the PEGylated nanoparticle in the salt solution do not differ significantly from that in water.

In the presence of the polymer melt (Figure 9(a)), the PEG polymers attached to the nanoparticle surface are stretched out to interact with surrounding polymers in the melt (not explicitly shown in the figure). In contrast, when the PEGylated nanoparticle is in the water environment, the PEG chains are collapsed on the nanoparticle surface or oriented in loops close to the surface; the chains are overall more coiled compared to in the polymer melt where they are stretched out. Attractive intermolecular interactions between PEG polymers cause them to stretch in the melt to network with surrounding PEG polymers. This attractive interaction causes them to coil close together on the nanoparticle surface in the presence of water. The decrease in average radius and R_g of the PEGylated nanoparticle in the presence of water is owed to this coiling due to PEG polymers being more attracted to each other than to water molecules, causing entanglement and coiling on the nanoparticle surface. This is shown clearly in Figure 9(b). The decrease in the average volume per grafted ligand in the water environment is consistent with the snapshots in Figure 9(b) where the PEG ligands are collapsed on the nanoparticle surface. The coiling of PEG ligands onto the nanoparticle surface results in a loss of conformational degrees of freedom for individual attached chains, leading to a lower volume available per PEG ligand. PEG chains with larger average R_g and $\langle R_{ee} \rangle$ values are consistent with chains stretched out away from the nanoparticle surface, consistent with Figure 9(a). In Table 5, there is a significant difference in $\langle R_{ee} \rangle$ values for the PEG chains; this is not the case for the average R_g values. The small standard deviation of the R_g values of individual PEG chains in the melt and in the water environment indicates that R_g values may not give an appropriate description to how the PEG chains are behaving in different environments; R_g values describe the overall space that the PEG ligand is contained in but is not useful to describe the average molecular configuration of the ligand in different environments.

Experimental and theoretical research groups who have studied PEGylated nanoparticles in water or in polymer melts have

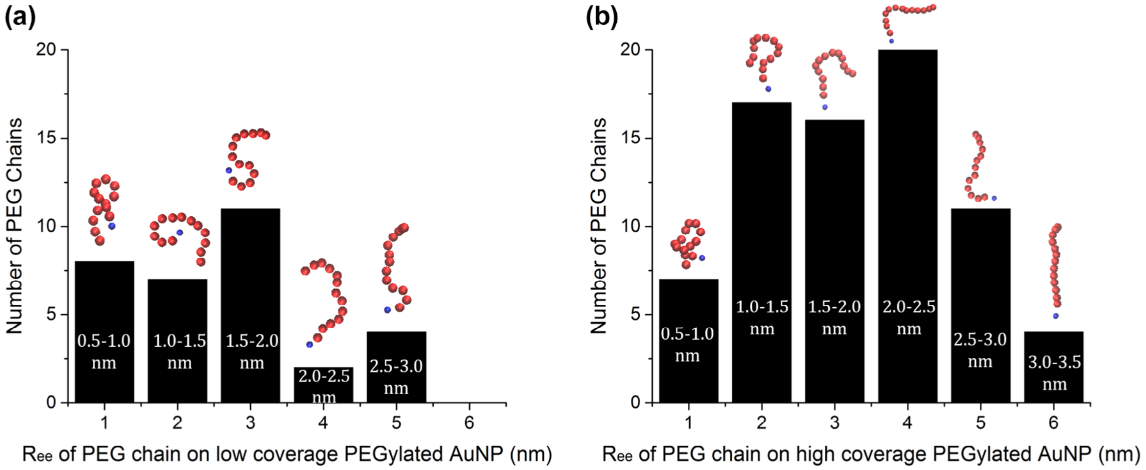

Figure 10. (Colour online) Distribution of R_{ee} of ligands on (a) PEGylated AuNP with (a) lower PEG coverage and (b) higher PEG coverage equilibrated in water. Snapshots of typical configurations from that distribution are included with blue representing the thiol atom and red the beads of the PEG ligand. These are averages over 1 ns after equilibration is complete. This figure reproduced from Ref. [64].

characterised the behaviour of PEG in the so-called 'mushroom' or 'brush' regimes and examined the dependence of grafting density of PEG for these regimes [67–71]. The mushroom regime is described as a case where surface coverage of PEG is low, and PEG chains are found to be collapsed on the nanoparticle surface. Low grafting densities of PEG yield individual PEG ligands with more conformational degrees of freedom. In PEGylated nanoparticles with high grafting density, the characterisation is brush regime, where individual PEG chains are likely to be stretched away from the nanoparticle surface in order to minimise steric repulsion and overall free energy of the system. Individual PEG chains on brush type PEGylated nanoparticles have lower volume available due to reduced conformational degrees of freedom.

In Figure 9, we see that there is no uniformity to the behaviour of ligands on the nanoparticle surface; a distribution of molecular configurations exists where some chains are coiled close to the nanoparticle surface while some chains are flattened and stretched out away from the nanoparticle surface. This gives rise to a distribution of individual $\langle R_{ee} \rangle$ values. As seen in Table 5, the standard deviations of the $\langle R_{ee} \rangle$ values for the PEG ligands in the melt and in water suggest that there exists a wide distribution of configurations that PEG ligands can assume, from the coiled to the stretched state. We illustrate this by providing the distribution of $\langle R_{ee} \rangle$ values for the ligands on a low-coverage and high-coverage example in Figure 10. For Figure 10(a) and (b) we examined each PEG ligand and binned them according to $\langle R_{ee} \rangle$ values, and we provide a molecular configuration of a typical PEG ligand found within each range of $\langle R_{ee} \rangle$ values. We find that in both cases of low and high coverages, a wide distribution of $\langle R_{ee} \rangle$ values exist, with a wider distribution occurring for the PEGylated nanoparticle with higher coverage. 'Mushroom' and 'brush' are terms which are inadequate to describe a ligand-coated nanoparticle since they imply more uniformity than the actual case.

The snapshots in Figure 9 alone suggest that on a given PEGylated nanoparticle, the PEG ligands are present in various configurations where the mushroom shape (curled and flattened on the nanoparticle surface), or PEG ligands with smaller $\langle R_{ee} \rangle$ values can exist alongside the brush-type (stretched out) PEG ligands with larger $\langle R_{ee} \rangle$ values. There is neither mushroom nor brush behaviour of PEG ligands in comparing nanoparticles with varying surface coverage density; in all cases, PEG ligands exist in multiple types of molecular configurations on the same nanoparticle. Only the distributions vary with coverage density.

The configuration of PEG ligands has been recently observed to vary in the presence of salt solution due to the favourable interaction of PEG ligands with sodium ions [72,73]. Utilising atomistic simulations, other groups have noted single PEG chains to wrap around sodium ions to form helical configurations [74,75]. In comparing the behaviour of the PEGylated nanoparticle in water to that in the salt solution from Table 5, we see that the characteristic values do not differ significantly. This indicates that the overall structure of the PEGylated nanoparticle does not change considerably in the presence of salt solution. We attribute this to the competition between various PEG chains in solution with the sodium ions in the environment. When multiple PEG chains are present, the sodium ions have a number of PEG beads where possible interactions occur and thus may not associate with an individual chain.

3.3. *Adsorption of nanoparticles at the interface*

The interaction of nanoparticles with membranes is of great interest to experimentalists who are designing nanocarriers for drug delivery applications [76,77]. These nanocarriers used in biomedical applications are often functionalised with biocompatible ligand groups that aid the passage of the nanoparticle through the body. Ultimately, the role of the nanocarrier is to reach targeted tissues and cells for therapeutic applications such as delivery of anti-cancer agents to cancerous areas in the body [78]. Polyethylene glycol is a widely used chemical group in biomedical drug delivery applications. The circulation time in blood of nanoparticles has been observed to increase due to functionalising with PEG groups [79]. This has led to investigations of the interaction of PEG with erythrocytes [80] since upon intravenous administration of PEGylated nanoparticles, the first cells these functionalised nanoparticles will come in contact with are erythrocytes [80]. Erthyrocytes, like other cells in the body, are comprised of many organelles protected by a lipid bilayer membrane. Nanoparticle permeation may cause disruption to the lipid membrane integrity and affect the passage of ions and other important molecules in and out of the cell. Damage to lipid bilayer membranes of erythrocytes or other important cells can result in *in vivo* cytotoxicity, which can result in cell death.

We have examined penetration of bare gold nanocrystals [53], alkanethiol-coated gold nanoparticles [33,81,82], and PEGylated gold nanoparticle penetration of a DPPC lipid bilayer membrane. These specific nanoparticles provide ideal model systems to gain an understanding of how the permeation process differs between a hydrophobic bare nanocrystal and two different functionalised nanoparticles, one containing a hydrophobic group that interacts favourably with the lipid tails and one containing a hydrophilic group that interacts favourably with the phosphate, choline and glycerol head groups of the lipid molecule. The permeation begins with the adsorption of the nanoparticle onto the membrane surface. The nanoparticle passes through the first lipid leaflet, is then engulfed by the membrane and is finally released from the lower membrane leaflet. In the following Figures 11–14, we display snapshots of the permeation process at these significant points for the bare gold nanocrystal, alkanethiol-functionalised and PEGylated gold nanoparticle. The results shown in the following figures compare permeation behaviour for nanoparticles with identical core size and functionalised nanoparticles with similar R_g. All snapshots displayed were obtained from permeation studies with the same nanoparticle velocity.

First, we consider how the adsorption process occurs. Snapshots from Figure 11(a), (c) and (e), were taken when the average position of the nanoparticle was 1.0 nm above the equilibrium position of the phosphate groups of the top membrane leaflet (where the nanoparticle has only partially penetrated the lipid–water interface). In Figure 11(b), (d) and (f), the top view of the choline groups from the top membrane leaflet are shown for the same position of the nanoparticle from Figure 11(a), (c) and (e).

Examination of the top view of the lipid head groups at the point of the first lipid–water interface Figure 11(b) shows that the top leaflet is intact and minor disturbance has taken place when the bare nanocrystal approaches the top leaflet of the bilayer membrane at the first lipid–water interface. The approach of the

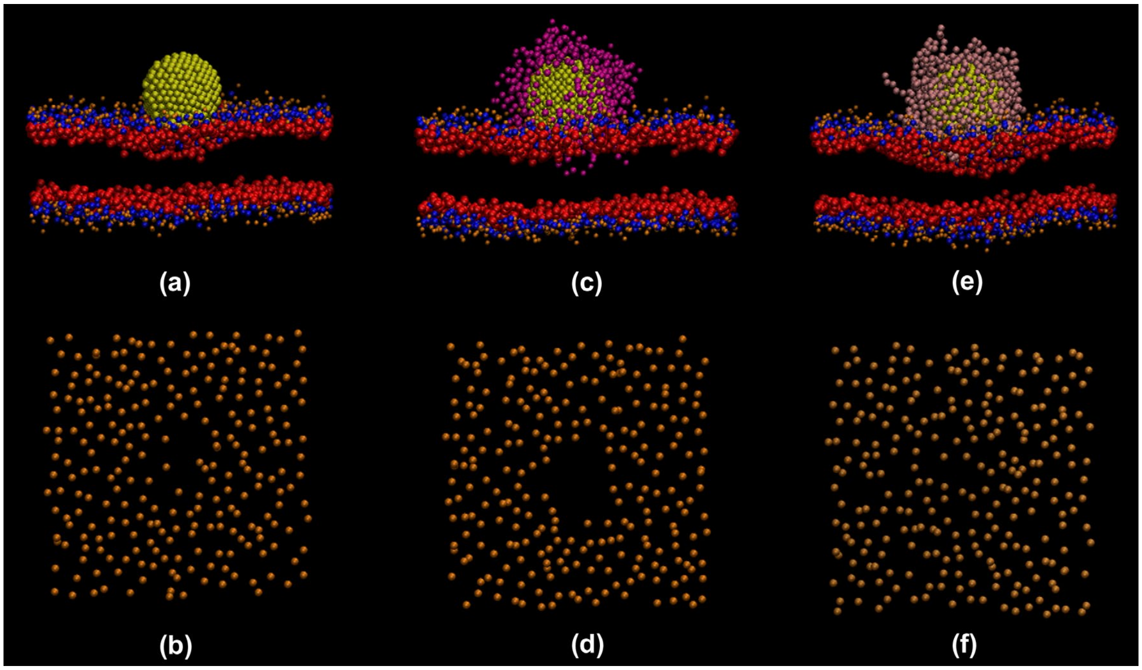

Figure 11. (Colour online) Snapshots of the (a, b,) bare nanocrystal, (c, d) alkanethiol-coated gold nanoparticle, and (e, f) PEGylated gold nanoparticle. Snapshots indicate (a, c, e) the approach of the nanoparticle to the top leaflet of the membrane, (b, d, f) the top view of the choline headgroups of the first membrane leaflet, Each set of snapshots contains omitted atoms (orange = choline, blue = phosphate, red = glycerol, green = alkyl tails, yellow = gold nanoparticle core, magenta = alkanethiol ligands, and pink = PEG ligands). Representation of groups in Figures 12–14 is the same as defined here.

alkanethiol-coated gold nanoparticle (Figure 11(c) and (d)) at the first lipid–water interface is significantly different from the bare nanocrystal in that it breaks through the lipid head groups and disturbs the integrity of the membrane. Head groups of the DPPC lipid bilayer membrane have an unfavourable interaction with alkanethiol ligands and are therefore pushed away from the leading ligands on the functionalised nanoparticle upon approach of the first membrane leaflet. In Figure 11(d), that the alkanethiol ligands have completely penetrated the lipid membrane and pushed the head groups far apart creating a hole in the top membrane leaflet. The hole in Figure 11(d) suggests a substantial change to the self-healing properties of the first lipid–water interface and its ability to resist penetration of foreign molecules and ions. In examining the approach of the PEGylated gold nanoparticle from Figure 11(e), we see that the top membrane leaflet begins to develop a slight curvature while still maintaining its integrity and continuity as a membrane leaflet. In contrast, Figure 11(f) shows that the PEG ligands have curved upward towards other PEG ligands and the nanoparticle core, leaving the top membrane leaflet intact. The curvature we observe is a possible explanation as to why experimentalists observe the receptor-mediated endocytosis of PEGylated nanoparticles and the wrapping of lipid bilayer membranes around such approaching nanoparticles [83,84]. The DPPC lipid bilayer membrane in our system is tethered at the edges and therefore, we cannot observe endocytosis in our simulations. The observation of the membrane curving around the PEGylated gold nanoparticle already indicates that lipid membranes are capable of wrapping around PEGylated gold nanoparticles more easily than the alkanethiol-coated gold nanocarriers due to a favourable interaction between the PEG ligands and lipid head groups. In vivo, endocytosis of such nanoparticles can take place as a receptor-mediated process; however, we anticipate that even without such special receptors, endocytosis may be feasible for nanoparticles with PEG ligands.

3.4. Nanoparticle penetration of the top leaflet

Once the nanoparticle has been adsorbed it begins to move into the membrane. We examine the behaviour as it is passing through the first membrane leaflet in snapshots from Figure 12(a)–(c) that show the bare nanocrystal, alkanethiol-coated gold nanoparticle and PEGylated gold nanoparticle, respectively, at the position of the equilibrated phosphate groups of the first bilayer membrane leaflet. In Figure 12(a) the bare gold nanocrystal has mostly penetrated through and continued to form an even larger hole in the membrane (evident in top view, not shown here). There are some choline groups surrounding the leading part of the gold nanocrystal forming a slight curvature of the membrane. Overall, the hole formed in the membrane shown in Figure 11(b) becomes larger since the bare nanocrystal is pushing apart the lipid head groups as it permeates the membrane. In Figure 12(b), we see that the alkanethiol ligands have pushed through the first leaflet completely in order to interact with the lipid tails to enhance favourable hydrophobic interactions; the membrane exhibits no curvature; the lipid heads hold an unfavourable interaction with the alkanethiol ligands and are pushed away from the nanoparticle during the permeation. In Figure 12(c), we see a significant curvature of the membrane where lipid head groups are essentially surrounding the PEGylated nanoparticle due to the favourable interactions between the hydrophilic PEG ligands and hydrophilic lipid head groups. At closer view, the PEG ligands are seen to curve upwards and towards the nanoparticle surface

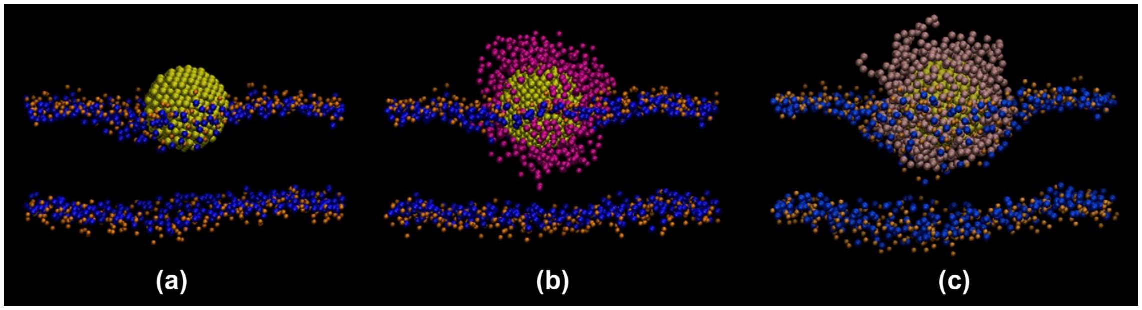

Figure 12. (Colour online) Snapshots of the (a) bare nanocrystal, (b) alkanethiol-coated gold nanoparticle and (c) PEGylated gold nanoparticle. Snapshots indicate (a, b, c) the nanoparticle within the top membrane leaflet.

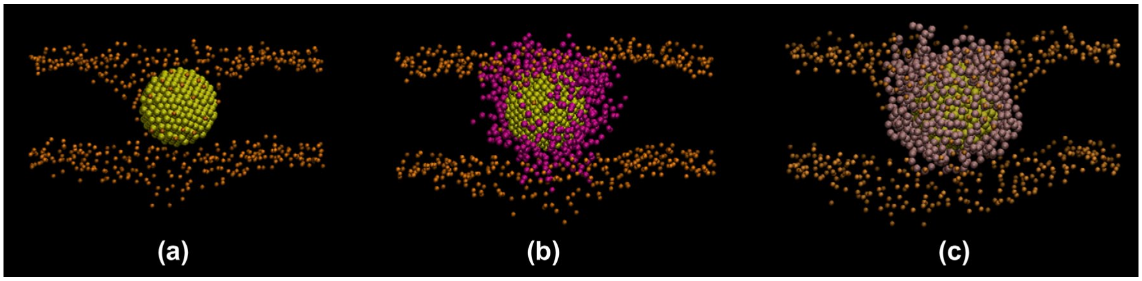

Figure 13. (Colour online) Snapshots of the (a) bare nanocrystal, (b) alkanethiol-coated gold nanoparticle and (c) PEGylated gold nanoparticle. Snapshots indicate (a, b, c) the nanoparticle located in the middle of the membrane.

and the interfacial region of the membrane to avoid interaction with the hydrophobic lipid tails.

3.5. Nanoparticle in the middle of the membrane

While hydrophobic ligands will maintain a favourable interaction with the lipid tails in the membrane interior, hydrophilic ligands will attempt to avoid interacting with the alkyl tails in the environment. Snapshots from Figures 13(a)–(c) highlight differences in behaviour of a bare gold nanocrystal and functionalised gold nanoparticle in the middle of the lipid membrane. Figure 13(a) shows that a few lipid molecules have been carried from both the top and the bottom layer and are surrounding the bare gold nanoparticle. The same has occurred in Figures 13(b) and (c), however the view is not clear since the ligands are also present in the snapshot. Note that whereas the alkane ligands have reached out to engage the hydrophobic tails, the PEG ligands have withdrawn away from the tails of the lipids and formed coils on the surface of the Au to avoid interactions with the hydrophobic units. We also see in Figure 13(c), a few PEG ligands interacting with the lipid head groups in the top and bottom membrane leaflet.

3.6. Nanoparticle penetration of the bottom leaflet

Once the nanoparticle has passed through the hydrophobic interior of the membrane, it begins the releasing stage as it begins to exit the second membrane leaflet. Figures 14(a)–(c) display the onset of the exit of the bare nanocrystal, alkanethiol-coated gold nanoparticle and PEGylated gold nanoparticle, respectively, at the second lipid–water interface. It is clear that DPPC molecules surround the bare nanocrystal and alkanethiol-coated nanoparticle upon exit. Lipid molecules surround the bare nanocrystal and move with it as it exits. We find in our simulations that some lipid molecules are carried into the bulk solution along with the bare nanocrystal while most return to the top membrane leaflet. The alkanethiol-coated gold nanoparticle drags many more lipid molecules into the bulk solution upon exit due to a favourable hydrophobic interaction between the lipid tails and alkanethiol ligands. In contrast to the bare nanocrystal, these lipid molecules do not return to the bilayer membrane but remain with the nanoparticle well after it exits the membrane. In Figure 14(c), we see that lipid molecules are not dragged by the PEGylated nanoparticle upon exit from the membrane. Given the less favourable interaction between the hydrophilic PEG ligands and hydrophobic lipid tails, hardly any lipid molecules are displaced from the membrane.

A smaller gold core would result in less damage overall to the membrane, especially in the cases of the bare nanocrystal and alkanethiol-coated gold nanoparticle. We found smaller diameter gold cores result in smaller induced pores upon permeation as well as allowing fewer lipid molecules to be dragged into the bulk solution. An alkanethiol-coated nanoparticle with higher grafting density and longer ligand lengths would result in a larger induced pore upon permeation and increased damaged to the lipid membrane; both result in more available favourable interaction sites with the hydrophobic tails and thus cause increased damage to the lipid membrane by removing even more lipid molecules upon exit from the membrane. A PEGylated gold nanoparticle with larger gold core and/or higher coverage density and/or longer ligand lengths would cause less damage to the membrane because lipid molecules would not be displaced upon exit from the membrane. We quantify these occurrences in the following sections.

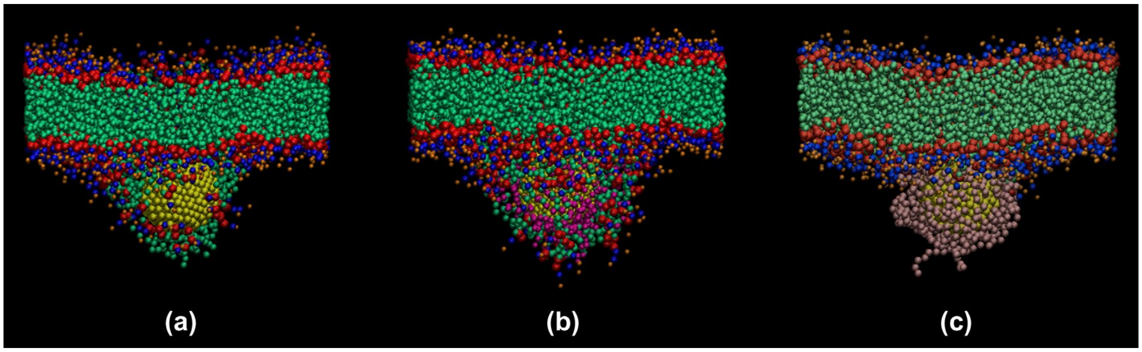

Figure 14. (Colour online) Snapshots of the (a) bare nanocrystal, (b) alkanethiol-coated gold nanoparticle and (c) PEGylated gold nanoparticle. Snapshots indicate (a, b, c) the nanoparticle exiting the membrane at the bottom leaflet.

3.7. Formation of a water string or pore and the subsequent expulsion of water from the centre of the membrane

The DPPC model membrane used in our permeation studies contains two aqueous compartments on either side of the lipid bilayer membrane. This effectively represents the intracellular and extracellular cell space with the lipid membrane protecting the intracellular components (organelles, other molecules). As we have shown clearly in Figures 11–14, nanoparticle permeation causes pores to form in the lipid membrane and as a result, water molecules present in the extracellular space can enter the membrane interior and may translocate past the inside leaflet and into the intracellular region as the membrane reseals. Observations from other investigators have indicated that nanocarriers permeating from extracellular to intracellular space are observed to induce defects in the membrane such as pores which allow water molecules to enter the hydrophobic membrane interior [85,86]. An excess of water molecules within a cell may cause lysing, and possibly result in cell apoptosis. This is an area of great interest to researchers in the biomedical industry who are designing nanocarriers for various applications and want to avoid unnecessary movement of water molecules into the cell interiors of non-targeted cells.

We compare water penetration resulting from permeation of the bare nanocrystal, alkanethiol-coated nanoparticle and PEGylated nanoparticle. For these three cases, we investigated the dependence of water penetration on nanoparticle permeation velocity, presence of ion concentration gradient, and ligand length and coverage density (which we display for the PEGylated case only). We have defined water penetration in all of our studies in the same manner; the number of coarse-grained water molecules found in the hydrophobic interior of the membrane in the course of nanoparticle permeation are regarded as ‘leaked’ water molecules. These water molecules may enter the hydrophobic membrane interior from both aqueous compartments. The water molecules located at the position of the phosphate head groups near the lipid and water interface are not included in this count.

We report in Figures 15–17 the number of water molecules present in the hydrophobic membrane interior under varying conditions, where the equilibrated positions of the phosphate head groups in the top and bottom membrane leaflets (the lipid–water interface) are indicated by green dashed lines. Complete membrane recovery in our system is achieved when zero water molecules are found in the membrane interior.

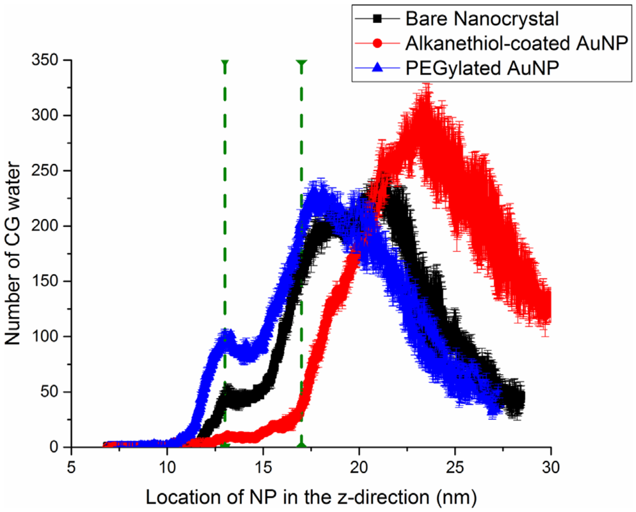

Figure 15. (Colour online) Number of coarse-grained water molecules that permeate into the hydrophobic membrane interior during permeation of a bare nanocrystal, alkanethiol-coated gold nanoparticle and PEGylated gold nanoparticle with the same permeation velocity. In this and succeeding Figures 16 and 17, the green dashed lines represent the equilibrated positions of the phosphate head groups at the top and bottom membrane leaflets. Each data point has error bars included based on three independent simulations.

In Figure 15, we compare the water penetration profiles of a bare nanocrystal, alkanethiol-coated nanoparticle and PEGylated gold nanoparticle, all with the same permeation velocity. These are the same cases considered in the snapshots of Figure 11–14, where all the gold cores are the same diameter and the alkanethiol-coated and PEGylated gold nanoparticle are nearly identical in overall size. We see from Figure 15 that the profiles for the bare nanocrystal and PEGylated gold nanoparticle are similar; the maximum occurs close to the equilibrated position of the second leaflet, and water molecules begin to exit the membrane soon after the nanoparticle exits the second leaflet completely. This maximum occurs earlier for the PEGylated nanoparticle. Since the bare gold nanoparticle is hydrophobic, it removes a few lipid molecules from the membrane, disrupting the membrane integrity and allowing water molecule entry to persist. From Figure 15, we see that the bare nanocrystal is less damaging than the alkanethiol-coated gold nanoparticle. For the alkanethiol-coated case, the

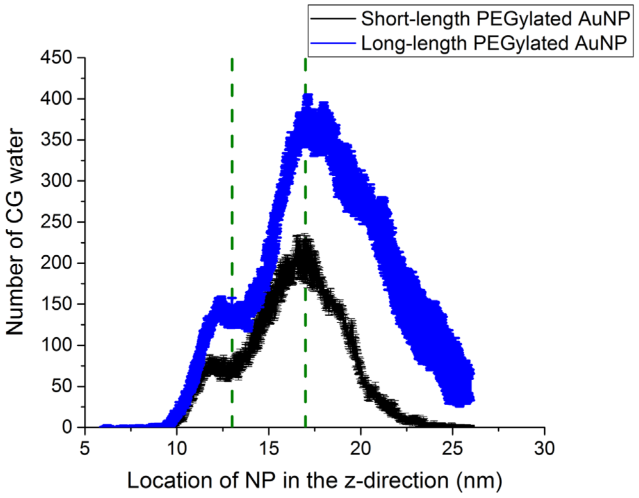

Figure 16. (Colour online) Number of coarse-grained water molecules that permeate into the hydrophobic membrane interior during PEGylated gold nanoparticle permeation, illustrating the effect of PEG length. The green dotted lines represent the equilibrated positions of the phosphate head groups at the top and bottom membrane leaflets. Each data point has error bars included based on three independent simulations. Figure reproduced from Ref. [64].

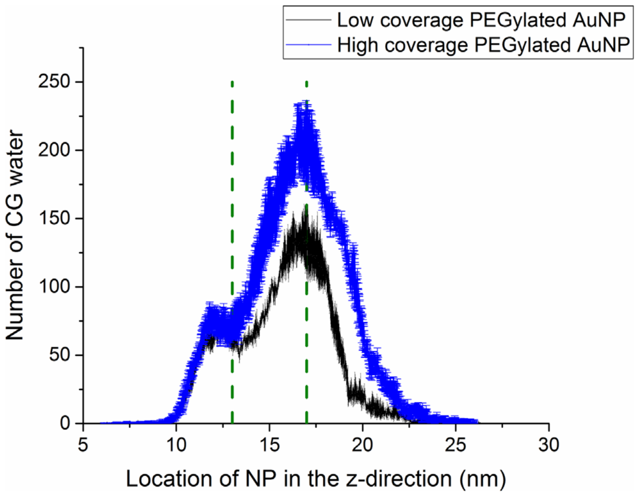

Figure 17. (Colour online) Number of coarse-grained water molecules that permeate into the hydrophobic membrane interior during PEGylated gold nanoparticle permeation, illustrating the effect of coverage density. The green dotted lines represent the equilibrated positions of the phosphate head groups at the top and bottom membrane leaflets. Each data point has error bars included based on three independent simulations. Figure reproduced from Ref. [64].

maximum occurs after the nanoparticle has completely exited the membrane. This is expected from the snapshot in Figure 14(c) where we observe that the alkanethiol-coated gold nanoparticle drags many lipid molecules along with it after the permeation, inducing a huge disruption in the membrane; thus, we expect that with the alkanethiol-coated case, expulsion of water occurs later and membrane recovery is slower.

In our study [82], we found that longer ligands in the alkanethiol-coated case induced more disturbance to the membrane leaflet and overall integrity of the membrane, which resulted in formation of larger water pores. Larger water pores increase the recovery time of the membrane since more water molecules can continue to penetrate the membrane interior and will take longer to be expelled into the aqueous compartments. As shown in Figure 16, the number of water molecules found in the hydrophobic membrane interior increases with increasing ligand length, for PEGylated nanoparticles as well.

We see in Figure 17 that water penetration increases for nanoparticles with higher surface coverage. Increasing the density of surface ligands on a nanoparticle increases its overall size [64]; a larger nanoparticle will induce a larger water pore in the membrane and allow more water molecules to enter the hydrophobic interior during permeation. From Figure 15, we observed that the bare nanocrystal was more damaging than the PEGylated case, although not significantly. Addition of hydrophilic ligands to the bare nanocrystal is thus less damaging since lipid molecules are not removed from the membrane. When compared to a bare nanocrystal with addition of hydrophobic ligands however, lipid displacement is significant and the membrane integrity is compromised.

In the case of the PEGylated nanoparticle, water molecules begin to enter the membrane interior even before the nanoparticle itself has permeated the first membrane leaflet as seen in Figures 15–17. This occurs since the PEGylated nanoparticle allows closely associated water molecules to move along with it near the membrane interior due to favourable hydrophilic interactions. This occurs, less significantly so with the bare nanoparticle, since unlike the alkanethiol-coated nanoparticle, it does not contain hydrophobic ligand entities to push water molecules away from the pore formed at the entrance to the membrane. This consequence of the hydrophobic alkanethiol ligands is demonstrated in Figure 15 where we see that few molecules enter the membrane interior until the nanoparticle has left the second membrane leaflet, whereupon water molecules enter. We had observed (Figure 14(b)) that upon exit, lipid molecules associate closely with the alkanethiol gold nanoparticle and do not immediately return to their equilibrated position after the nanoparticle exits; a large pore is formed where water molecules can continue to permeate the membrane interior. Water molecules do not begin to leave the membrane interior until well after the nanoparticle has exited the membrane, showing signs of slow recovery. Overall, our examination of water penetration demonstrates that highly hydrophobic nanoparticles will not only allow many water molecules to permeate the membrane interior, they hinder the self-healing recovery of the membrane, thus possibly damaging the cell in a likely permanent way. In some cases with longer ligands and higher surface coverages of alkanethiol on gold nanoparticles, if too many lipids have been dragged into the bulk solution, the membrane may not be able to recover at all.

3.8. *Passage of ions during nanoparticle permeation events, mechanism by which this occurs*

Natural biological systems include ions in the extracellular and intracellular compartments which are present at well-regulated concentrations. This concentration, in addition to the electric potential across the membrane, plays an integral role in regulating the entry and exit of certain ions into cells [87]. In biological environments, ion permeation across lipid bilayer membranes normally occurs by a transmembrane protein pore-mediated process or with assisted transport for ions that cross from the extracellular to intracellular cell space. Since we observed water molecules to penetrate the membrane interior, we expect ions to be able to translocate to the other aqueous compartment via the water pore formed by nanoparticle permeation.

We examined the penetration of ions across a lipid bilayer membrane as a consequence of nanoparticle permeation by a bare gold nanocrystal, alkanethiol-coated gold nanoparticle and a PEGylated gold nanoparticle. In these systems, an unequal ion concentration gradient was implemented by adding sodium and chloride ions to the top aqueous compartment of the bilayer membrane system at a concentration less than the saturation limit of sodium chloride in water. The system contained two walls cut from an FCC structure and placed on either side of the system; these walls were impermeable to ions and water and isolate the ions in the top compartment (ions that would otherwise move to the bottom compartment due to periodic boundary conditions).

Ions already present in the top compartment of the lipid bilayer membrane system cannot translocate to the other compartment on their own due to a resistance present at the lipid–water interface against such a permeation; this is a direct result of the Columbic interaction between the ions and phospholipid head groups. The interior of the lipid membrane being highly hydrophobic also prevents translocation of ions. In previous theoretical investigations [88–92], a 'water finger' or chain of linked water molecules has been observed to protrude across the lipid membrane through a water pore connecting the aqueous compartments to one another. Atomistic simulations from various groups [88,89,93], in agreement with our findings, have shown ions to permeate across the lipid membrane by traveling along the water molecule network formed across the water pore induced by nanoparticle permeation in the lipid membrane. It has been observed previously that chloride ions are able to integrate into these water molecule networks easily due to its lower surface charge density and increased flexibility of the hydrated ion. Many studies, including those from our previous work, indicate that chloride ions have a tendency to stay close to the interfacial region while sodium ions concentrate near the phospholipid head groups [81,88]. This supports our observations that overall, more chloride ions tend to translocate across the lipid membrane as compared to sodium ions, in cases of bare and ligand-coated nanoparticle permeation.

Since the formation of the water finger is vital to the ion translocation process, we examined the behaviour of water molecules at the instant of time where the number of water molecules found in the membrane interior is at a maximum. In Figure 18(a), for the bare gold nanoparticle a visible water finger is formed, in which a few ions will travel along to permeate through the membrane. In Figure 18(c), we do observe a water column formation as well because PEG ligands associate favourably with water molecules during the permeation. This water molecule chain however is not long-lived (as shown in our previous studies); therefore most ions that enter that water pore, similar to the case of the bare nanocrystal, return to the bulk solution as the membrane begins to recover. Overall, in the cases of both the bare nanocrystal and PEGylated gold nanoparticle, we found that ion penetration events were sensitive to larger effective nanoparticles either in size of gold core, or overall size of functionalised nanoparticle with different ligand lengths and/or grafting densities. Longer ligand lengths and higher grafting densities both resulted in larger effective nanoparticles which induced larger water pores in the membrane, thereby allowing more ions to enter the interior and travel to the opposite compartment. For the PEGylated gold nanoparticle, the PEG ligands cause minimal disturbance to the membrane, since lipids are not dragged by the nanoparticle and the membrane is allowed to recover immediately after permeation of the first membrane leaflet. This drives ions to return to the region near the phospholipid head groups at the interfacial region.

We observed few to no ion transport events to take place during permeation of the alkanethiol-coated gold nanoparticle. This is consistent with our observation and snapshot from Figure 18(b) where we see no noticeable formation of a water column. During permeation of an alkanethiol-coated gold nanoparticle, the long mobile ligands push lipid head groups and water molecules away from the nanoparticle due to unfavourable interactions. This does not allow formation of a water column and thus few to no ions are able to permeate the lipid bilayer, despite the formation of a hole in the top leaflet as the nanoparticle enters the membrane.

3.9. Lipid flip-flop events accompany nanoparticle permeation and with potential for leaflet composition changes

Lipid molecule flip-flop occurs when a lipid molecule translocates from one leaflet of a bilayer membrane to the other leaflet

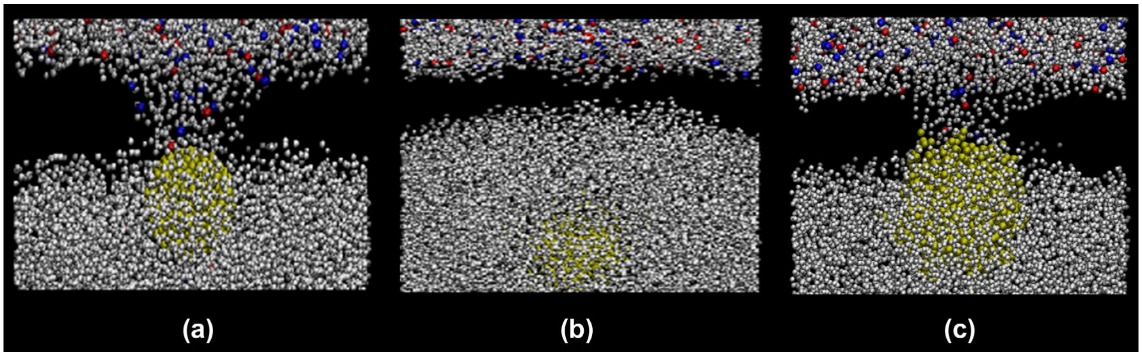

Figure 18. (Colour online) Snapshots of the (a) bare nanoparticle, (b) alkanethiol coated nanoparticle, and (c) PEGylated nanoparticle at the position where the maximum amount of water molecules are found in the membrane interior. Gold = nanoparticle core and ligands, white = CG water molecules, blue = sodium ions and red = chloride ions.

across a defect in the lipid bilayer. These defects or pores are often induced by external penetration of foreign molecules and can be a consequence of nanocarrier permeation, as we have shown. Lipid flip-flop is a natural biological process supported by lipid translocators, either integral or transmembrane proteins, or by specific enzymes (flipases) that can catalyse lipid flip-flop [94]. Experimentally, it has been observed that specific peptide molecules can accelerate the frequency of lipid flip-flop events through membrane pores containing peptides and lipid molecules [95]. Lipid membranes are asymmetric in nature and unwarranted lipid translocation can influence the molecular recognition capabilities of the outer bilayer membrane surface [96]; this can have damaging effects on the lifetime of biological cells. We observed lipid flip-flop events in our simulations, as lipid molecules are displaced from the top membrane leaflet during permeation of the bare, alkanethiol, and PEGylated gold nanoparticles and eventually re-join the other leaflet. The penetration by these nanoparticles, albeit different in chemical properties, still caused movement of lipid molecules from the top membrane leaflet during the adsorption and permeation of the first leaflet steps. We studied the mechanism by which lipid flip-flop occurs and the factors that affect the number of such events.

We defined lipid flip-flop events to occur when a lipid molecule originally present in the top leaflet, is found in the bottom leaflet (or vice versa) after permeation is complete and the membrane has recovered to its equilibrium situation. In our studies with bare nanocrystals, we observed that the number of lipid flip-flop events increased with increasing nanoparticle size. An increase in core diameter results in larger pore formation in the membrane; this allows more lipid molecules to move into the water pore and have the potential to complete a lipid flip-flop. Larger functionalised nanoparticles tend to disturb the membrane more during permeation and have propensity to displace more lipid molecules, therefore giving rise to more lipid flip-flop events. In the case of the alkanethiol-protected gold nanoparticles, we observed few to no instances of lipid flip-flop. On the other hand, we observed that lipid translocation increased with longer ligand lengths and increased surface coverage density of PEG. We found that longer PEG ligands cause greater disturbances to the membrane bilayer leaflets during the nanoparticle permeation; this resulted in more instances of lipid dislocation from the membrane, resulting in completion of a lipid flip-flop. For nanoparticles with increased coverage density, more ligands can disturb the top layer of the membrane during permeation and thus, larger numbers of lipid molecules are translocated. We observed lipid molecules to also flip-flop from the bottom leaflet of the membrane to the top leaflet; this was unique to PEGylated gold nanoparticles. We did not observe this particular phenomenon in the case of the bare gold nanocrystal or the alkanethiol-coated gold nanoparticle.

We examined the mechanism by which the flip-flop occurs; in Figure 19 are snapshots of typical lipid flip-flop events that take place as a consequence of PEGylated gold nanoparticle permeation. We show lipid molecules translocating from the top membrane leaflet to the bottom membrane leaflet in Figure 19(a) and (b) and translocating from the bottom membrane leaflet to the top membrane leaflet in Figure 19(c) and (d). These snapshots indicate that the mechanism of lipid flip-flop does not differ whether it originates from the top membrane leaflet or the bottom membrane leaflet; in both cases, the lipid molecule will fully reorient itself in the z-direction, translating through the pore formed by the intruding PEGylated gold nanoparticle. As it joins the opposite membrane leaflet, it has undergone complete reorientation. For lipid flip-flop events occurring as a consequence of bare gold nanoparticle permeation, this same reorientation mechanism was observed as well. Only a few lipid molecules complete a flip-flop from the bottom membrane leaflet as a consequence of PEGylated nanoparticle permeation with short PEG lengths, at any coverage. For PEGylated gold

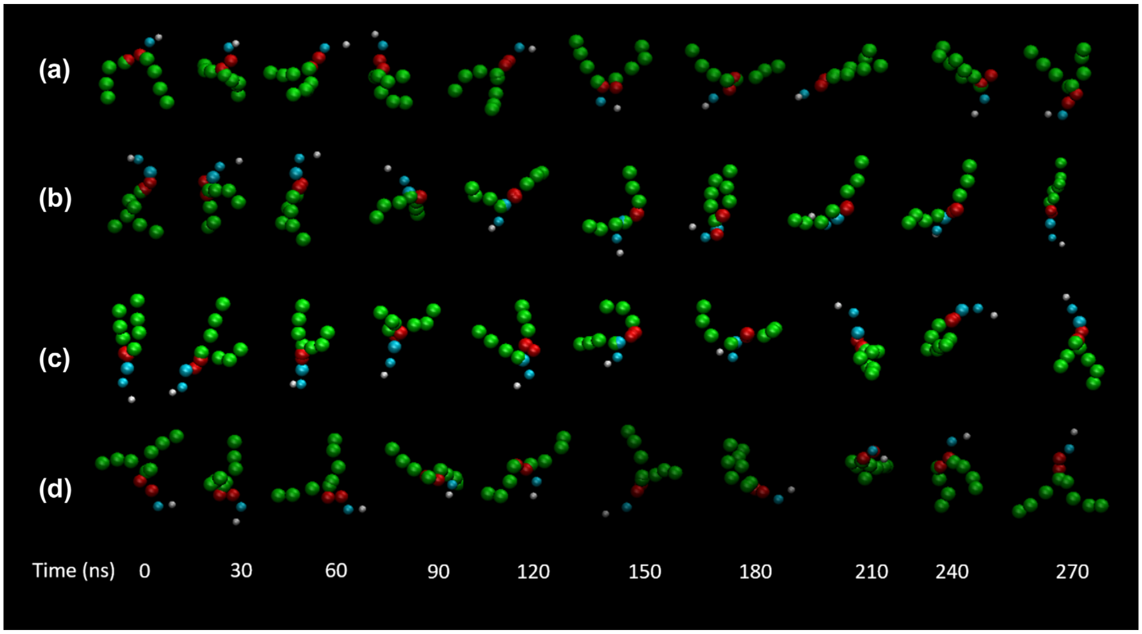

Figure 19. (Colour online) Snapshots of lipid flip-flop events from the top leaflet (a, b) and bottom leaflet (c, d) of the membrane with a PEGylated gold nanoparticle with permeation velocity of 0.075 m/s figure reproduced from Ref. [64].

nanoparticles with longer PEG ligands and higher surface coverage densities, there are higher incidences of lipid translocation from the bottom membrane leaflet. Larger nanoparticles with longer ligand lengths and increased surface coverage densities cause larger perturbations to both the top and bottom membrane leaflet even at the early stages of the permeation while the nanoparticle core is at the position of the top membrane leaflet. These perturbations cause many lipid molecules to be displaced from their original position and result in lipid flip-flop originating from both leaflets. For the lowest nanoparticle permeation velocities, the incidences of lipid flip-flop events are few; less than 3% of the total lipids in the bilayer membrane translocated to the other leaflet as a result of PEGylated nanoparticle permeation.

3.10. Displacement of lipids from the membrane itself

We observed in Figure 14(c) that many lipid molecules are still associating closely with the alkanethiol-coated nanoparticle upon leaving the lower membrane leaflet. When we followed the alkanethiol-coated nanoparticle after it had left the lower membrane leaflet, we found that a majority of the lipid molecules dragged along by the nanoparticle did not return to the membrane leaflet to complete a lipid flip-flop (unlike in the bare gold particle case). Instead, we found that most of the lipid molecules associated with the alkanethiol-coated nanoparticle were dragged into the bulk solution and did not return to the membrane. We examined the molecular mechanism by which a lipid molecule is displaced as a consequence of nanoparticle permeation. We found that the lipid tails open and close frequently within the alkanethiol ligand space, indicating close interaction with the mobile alkane chains. We found that this occurs by means of the lipid molecule tails becoming entangled in the alkane chains attached to the nanoparticle. Once this entanglement occurs, the lipid tails adhere to the nanoparticle and are displaced from the membrane instead of completing the lipid flip-flop. In Figure 20 [64], we show snapshots of the mechanism by which a lipid molecule from the bilayer membrane is carried into the bulk solution after entangling with alkanethiol ligands on the nanoparticle.

In Figure 20, we have identified a group of ligands that are contained within the interaction volume of a particular lipid molecule. This lipid entangles with a pair of ligands located near the lipid tails and is subsequently dragged by the nanoparticle into the bulk solution. Interestingly, this arrangement mimics the configuration a lipid molecule would have in a bilayer membrane where it is surrounded by other hydrophobic tails. Owing to the favorability of the hydrophobic interaction between the alkanethiol ligands and lipid tails, the ligands on the nanoparticle essentially compete with the surrounding lipid tails for interaction with the lipid molecule. If the lower leaflet wins, a flip-flop event completes. Otherwise, entanglement results in lipid displacement from the membrane. This entanglement effect becomes more critical with nanoparticles that are larger and/or have longer hydrophobic ligands. For this reason, we observe much fewer flip-flops to take place with nanoparticles containing longer hydrophobic ligands where lipid displacement is the dominant consequence as a result of permeation with an alkanethiol-coated nanoparticle.

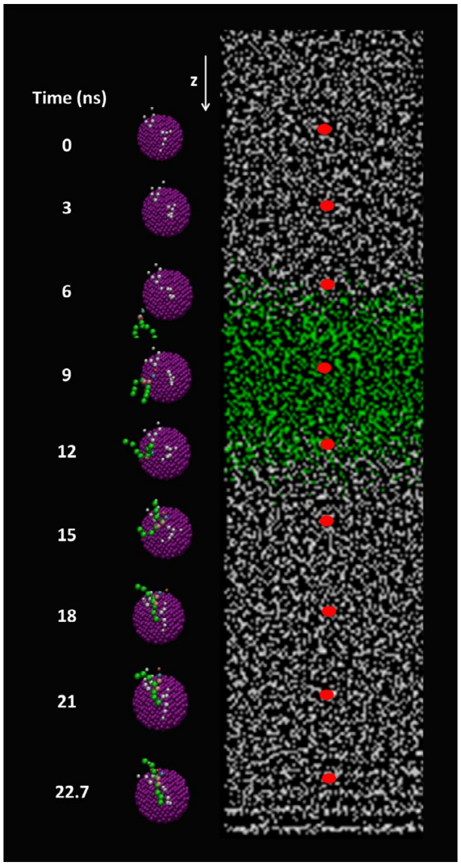

Figure 20. (Colour online) Snapshots of mechanism of lipid displacement from a bilayer membrane driven by entanglement of lipids in the alkanethiol ligands. The red dots represent the position of the nanoparticle in the system at each snapshot; for clarity, other molecules and ligands on the nanoparticle are not shown. Figure reproduced from Ref. [82].

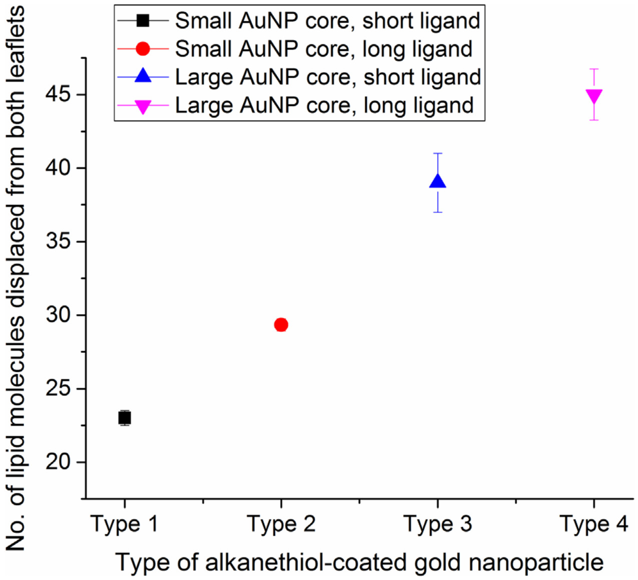

Figure 21. (Colour online) Number of lipid molecules lost from both membrane leaflets as a function of type of alkanethiol-coated gold nanoparticle where Type 1 = small diameter gold core and short ligand length, Type 2 = small diameter gold core and long ligand length, Type 3 = large diameter gold core and short ligand length, and Type 4 = large diameter gold core and long ligand length. The error bars are based on three independent simulations.

In Figure 21, we the quantify lipid molecules that have been lost from both the top and bottom bilayer membrane leaflets as a function of type of nanoparticle with differing core size and ligand length. We observe that nanoparticles with longer ligands cause more displacement of lipids from the membrane; the longer ligands enhance the hydrophobic interactions between the ligands and lipid tails and allow for entanglement to be more favourable. Also, we observed more incidences of lipid displacement for permeation by larger nanoparticles. Larger nanoparticles, having increased surface area, can extract more lipids from the membrane owing to the larger water pore formed during permeation, which disturbs the membrane leaflets. Overall, we observed more lipid molecules to be lost from the lower membrane leaflet compared to the top leaflet, which is consistent with results on a computational investigation of single-walled carbon nanotube permeation of DPPC lipid bilayer membranes [97]. The bare nanoparticle studied has been found to cause lipid displacement as well, but these events are far fewer compared to those with the alkanethiol-coated nanoparticle. On the bare nanoparticle, the lipid molecule adheres to the gold surface, essentially mimicking the role of a ligand. In these situations, the lipid head of the displaced lipid tends to face the nanoparticle surface with the tails pointing away, which favours the completion of lipid flip-flop as opposed to a lipid extraction. With the alkanethiol-coated nanoparticle, the lipid molecules tend to entangle closely with the alkane chains, with the lipid head groups facing outward, favouring lipid displacement. We observed that greater numbers of lipid molecules are displaced from the membrane at smaller permeation velocities. Even though some permeation velocities studied here are slightly higher than velocities used in experimental settings, this indicates that lipid molecule removal will likely occur in many experimental studies such as in drug delivery. The loss of lipid molecules in some cases may be more harmful to the membrane compared to lipid flip-flop, and possibly result in cell death if the membrane is unable to recover. In PEGylated nanoparticle permeation, we do not observe lipid displacement to occur at all, indicating that nanoparticles with hydrophilic ligands are potentially more useful as nanocarriers for therapeutic or biomedical applications.

3.11. Steps towards membrane recovery after nanoparticle penetration

After nanoparticle permeation is complete, the membrane recovery process begins. Water molecules are expelled from the membrane since the hydrophobic interior is not favourable for water molecules. Membrane recovery can be achieved only when all water molecules have left the membrane interior; thus we investigated the time it takes for water molecules to be expelled after permeation by various nanoparticle types. Membrane recovery also requires that lipid molecules tend towards their equilibrium position where the preferred configuration is with the hydrophilic head groups facing the aqueous compartments and the hydrophobic tails packed together.

We return to the same examples where we examined the bare gold nanocrystal, alkanethiol-coated gold nanoparticle and PEGylated gold nanoparticle and quantify the number of water molecules present in the hydrophobic membrane interior as a function of time during nanoparticle permeation (Figure 22). We see that in the case of the PEGylated gold nanoparticle, water molecules begin to leave the membrane interior as soon as the nanoparticle crosses the second membrane leaflet in the bilayer. This indicates that the recovery process begins immediately as the PEGylated nanoparticle exits the membrane, at around 50 ns. The bare nanoparticle crosses the second membrane leaflet, and at about 70 ns, the water molecules begin to exit the membrane interior. We showed in the snapshots that the bare nanoparticle does disrupt the membrane by dragging lipid molecules away from the bilayer membrane (though not nearly as significantly as in the alkanethiol-coated case) which explains why water molecules continue to penetrate the membrane interior. The most significant difference is in the alkanethiol-coated case where the water molecules do not begin to exit the membrane until about 90 ns, i.e. 40 ns longer than it took for water molecules to exit in the PEGylated case. In some instances of alkanethiol-coated nanoparticles with larger cores and longer ligands, too many lipid molecules may be removed from the membrane, which cause significant disruption and does not allow the membrane to recover. In Figure 22, we see that even after the alkanethiol-coated nanoparticle has exited the membrane at (120 ns), water molecules remain in the interior. They are eventually expelled after 200 ns. Membrane recovery times may be important when nanocarriers are used in drug delivery applications.

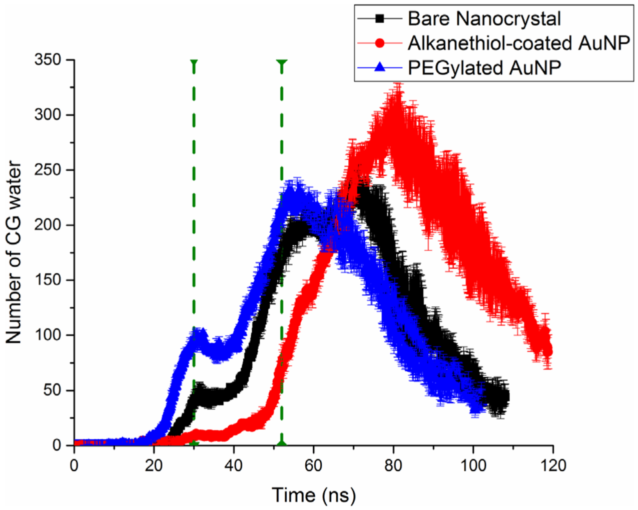

Figure 22. (Colour online) Number of coarse-grained water molecules that permeate, with respect to time, into the hydrophobic membrane interior during permeation of a bare nanocrystal, alkanethiol-coated gold nanoparticle, and PEGylated gold nanoparticle. The green dotted lines represent the equilibrated positions of the phosphate head groups at the top and bottom membrane leaflets. Each data point has error bars included based on three independent simulations.

3.12. Rotational behaviour of nanorods in lipid bilayers during permeation

The variety of nanoparticle shapes available in the biomedical industry has given rise to many types of functionalised nanoparticles with different impacts on biological pathways due to the size and shape of these nanocarriers [98–100]. Recently, gold nanorods have become popular in the drug delivery industry for applications ranging from phototherapy [101] to the direct targeting of cancer cells [102]. For this reason, we studied the

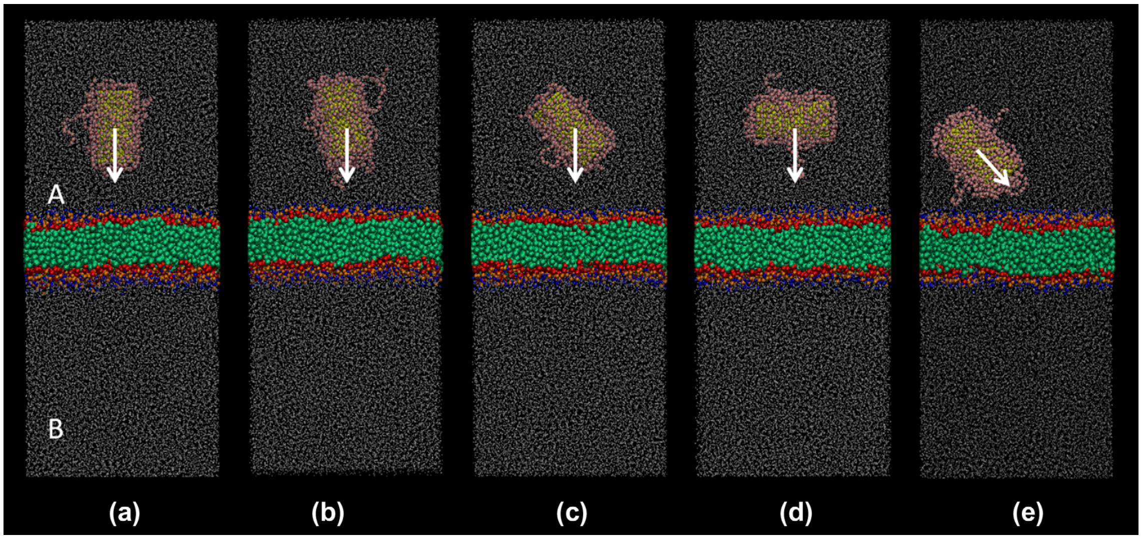

Figure 23. (Colour online) DPPC lipid bilayer membrane simulation system for investigation of PEGylated gold nanorod permeation from the top compartment (A) (or the extracellular membrane compartment) to the bottom compartment (B) (or the intracellular membrane compartment) across a DPPC lipid bilayer membrane where the initial angle to the membrane is varied by (a) 0°, (b) 10°, (c) 45°, and (d) 90°; (e) 45° where another method of permeation was employed (blue = choline, orange = phosphate, red = glycerol, green = lipid tails, white = water, gold = nanorod core, pink = PEGn-SH ligands). Figure reproduced from Ref. [103] higher grafting densities (0.89 ligands/nm^2) were obtained by Kinnear and colleagues [105]. Since our PEGylated goldnanorods with short and long PEG ligands had grafting densities (0.5–0.9 ligands/nm^2) comparable to that obtained experimentally by Kinnear et al., we used these in our simulations for permeation of a DPPC lipid bilayer membrane by PEGylated gold nanoparticles with aspect ratio > 1.

permeation of our model DPPC lipid bilayer system by a gold nanorod, functionalised with PEG ligands [103].

For comparison with our previous work on PEGylated spherical gold nanoparticles [64], we chose the volume of the gold nanorod core to be identical to the spherical core. We obtained PEGylated gold nanorods with short and long PEG ligands by completing a cycled annealing procedure with the same protocol as was used to construct our PEGylated spherical gold nanoparticle [103]. We obtained PEGylated gold nanorods with lower coverage densities than the spherical gold nanoparticle of the same volume. Experimentally synthesised gold nanorods [104] have been found to have much lower coverage densities compared to their spherical counterparts (e.g. 0.052 ligands/nm^2 compared to 1.63 ligands/nm^{2,} respectively. Recently, however,

We show in Figure 23 the set-up of our system where we examined a PEGylated AuNR pulled across the lipid membrane under constant velocity in the direction of the arrows for a PEGylated gold nanorod to permeate from the extracellular (compartment A) to the intracellular space (compartment B). We maintain a consistent system set-up as we had used for the bare nanocrystal, alkanethiol-coated nanoparticle, and PEGgylated spherical nanoparticle. There are, however, unique aspects to permeation by a nanorod-shaped particle. The angle at contact (entry angle) between the nanorod axis and the membrane surface may differ among a set of experiments, with possibly distinct outcomes. Similar to our simulations with spherical gold nanoparticles, the centre-of-mass of the nanorod is moved at a small constant velocity towards the membrane, allowing the nanorod to rotate about its centre-of-mass during permeation. In Figure 23, we show two approach methods we used. In the first approach, Method 1 (Figure 23(a)–(d)), we move the centre-of-mass of the nanorod along the direction normal to the membrane surface and vary the initial entry angle. In another approach, Method 2 (Figure 23(e)), we apply a constant velocity to the centre-of-mass such as to maintain the ratio of the normal and transverse velocity components. This still permits the nanorod to rotate about its centre-of-mass; however, it has a fixed pulling velocity vector along the direction of the original entry angle. We examined a range of constant velocities and initial angles for Method 1; and in Method 2, we investigated the effect of a pulling velocity vector with angle of 45°.

Many experimental studies indicate that the internalisation rate of PEGylated nanorods is affected by their entry angle relative to the lipid membrane surface [106]. Consequently, in our simulations, we examined the molecular mechanisms of nanorod permeation by following the permeation trajectory and noting its dependence on angle of entry. In a situation where many nanorods may permeate a bilayer membrane, the statistically least likely angle of approach would be 0° to the membrane normal. For a collection of AuNRs entering a membrane with various thermal velocities, at a distribution of entry angles, the paths taken by the AuNRs will be found among the various trajectories that we have observed for various entry angles while pulling along the normal to the membrane surface, together with those trajectories resulting from pulling the centre of mass along various angles. A complete set of all these trajectories constitute the distribution of trajectories for permeation of a membrane surface by a collection of PEGylated AuNRs having a distribution of thermal velocities and having a distribution of initial orientations relative to the membrane surface.

In comparing multiple simulations, we tracked the tilt angle of the nanorod axis relative to the membrane normal along the course of the permeation to investigate whether there is a pattern in the permeation trajectory and if this is dependent on entry angle. We show in Figure 24, the changing tilt angle, along the course of the nanorod permeation; independent simulations were studied so that multiple permeation pathways could be analysed.

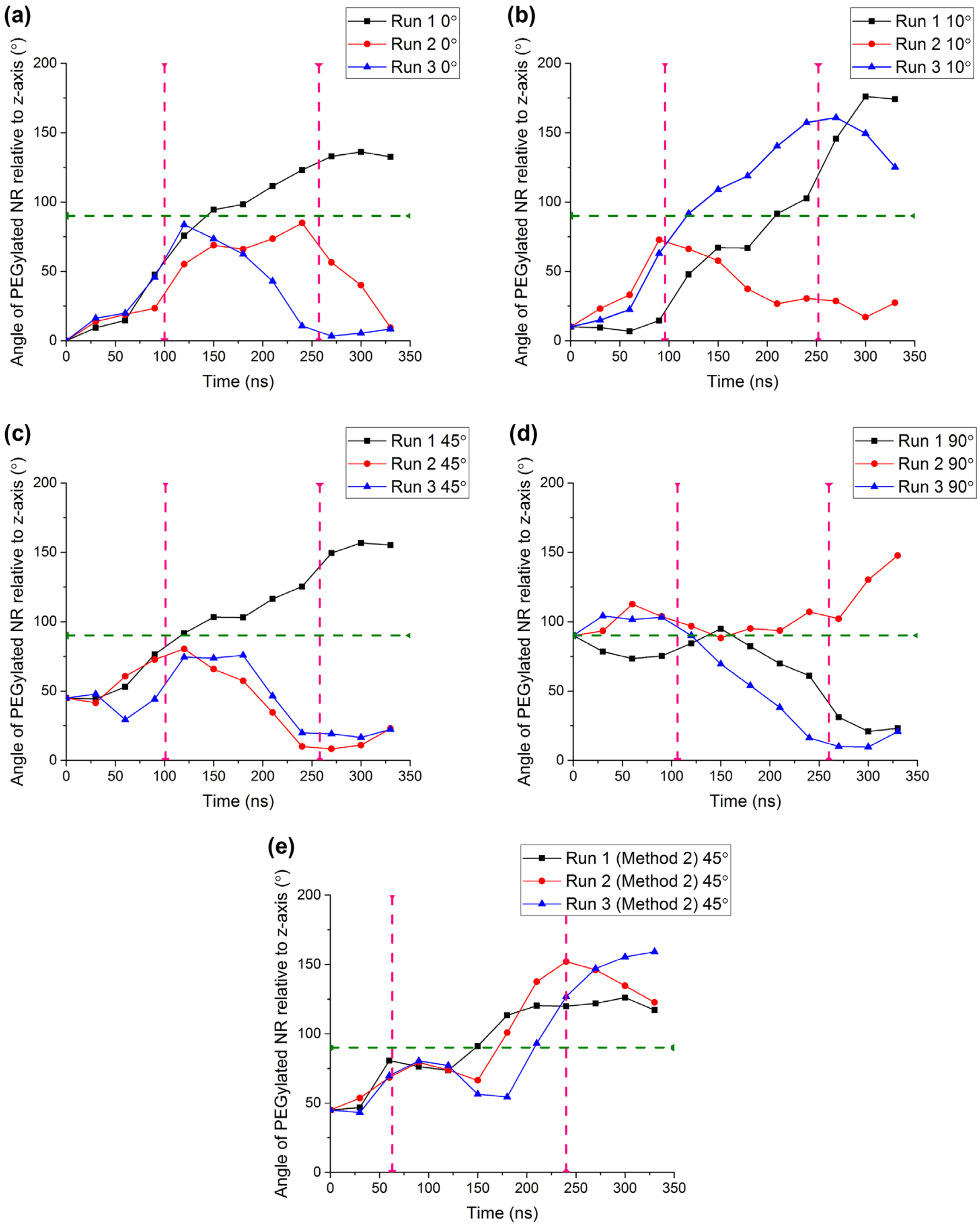

Figure 24. (Colour online) The tilt angle from the *z*-axis (normal to the membrane surface) of the nanorod axis is shown for each starting by (a) 0°, (b) 10°, (c) 45°, (d) 90° and (e) 45° at zero time. Data from three independent simulations are shown as individual runs. The green dotted line represents the angle at which the nanorod is perpendicular to the *z*-axis (in a plane parallel to the membrane surface or, lying down) and the pink dotted lines represent the time when the centre-of-mass atom of the PEGylated nanorod is 2.0 nm above from the top membrane leaflet and later, when it is 2.0 nm below the bottom membrane leaflet. Reproduced from Ref. [103].

We see from Figures 24(a)–(d), in simulations where the initial entry angle is 0°, 10°, 45° and 90° normal to the membrane surface, that there is a great variety in the trajectories taken by the nanorod starting from the same entry angle; but all trajectories have two things in common: (a) The tilt angle passes through or close to 90°, where the nanorod is lying down parallel to the membrane surface (indicated by the green dashed line). (b) Upon exit (the second pink dashed line corresponds to the time point when the centre-of-mass of the nanorod core is 2.0 nm away from the lower leaflet of the membrane), the tilt angle comes close to 0° or 180°, signifying the straightening up of the nanorod during exit.

The rotational pathway of nanorods in lipid membranes is more clearly shown in a 3D cartoon representation. One each of

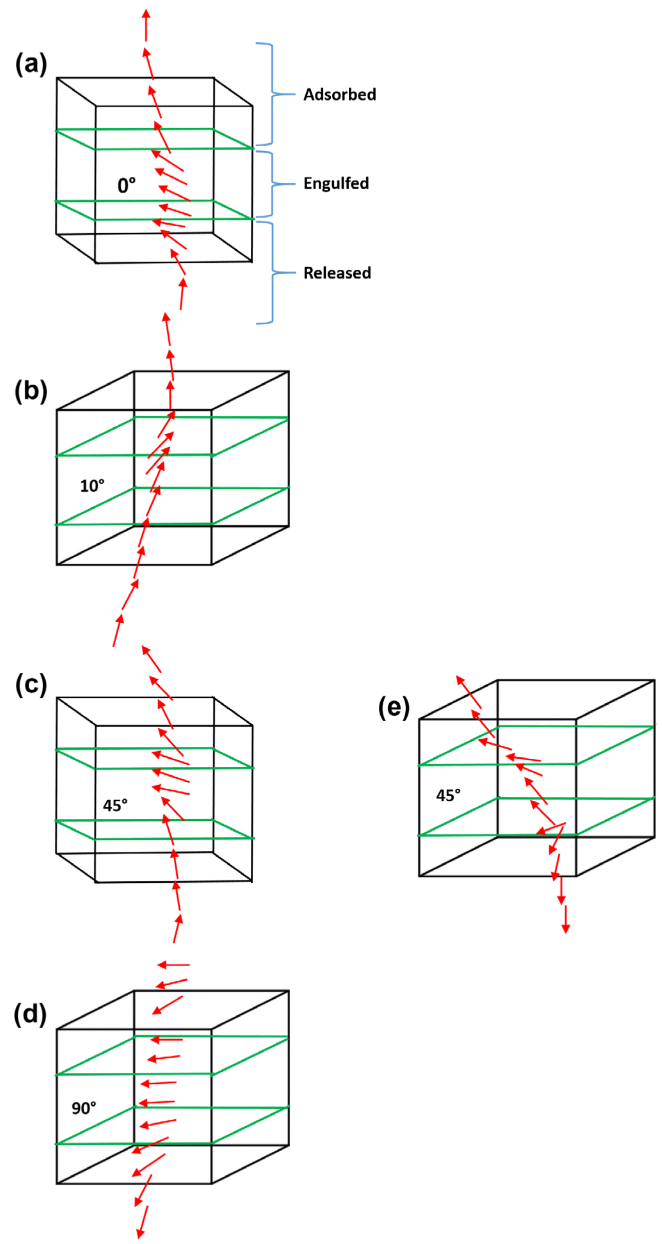

Figure 25. (Colour online) Cartoon representation of permeation of a PEGylated gold nanorod in the lipid bilayer membrane at low velocity and various initial angles. The green planes represent the equilibrated position of the phosphate groups in the top and bottom membrane leaflets. Initial angles by (a) 0°, (b) 10°, (c) 45°, (d) 90° and (e) 45°. Each arrow is at 30 ns intervals starting with 0 ns. Reproduced from Ref. [103].

those trajectories in Figures 24(a)–(e) is depicted in Figure 25; for various initial angles, along the course of the permeation, the change in orientation of the nanorod (represented by the red arrow) in three-dimensional space show general similarities. We can consider the trajectory to occur in three stages; first the nanorod is adsorbed on the membrane surface, then engulfed where it fully enters the membrane, and finally it is released by the membrane. While Figure 24 shows only the change in tilt angle relative to the normal to the membrane surface in the x–y plane, our cartoon representations in Figure 25 show that the nanorod also turns in the x–y plane during the course of the permeation. Comparing Figure 25(c) and (e), we see that the trajectories are very similar even though in (c) the nanorod is approaching along the normal to the membrane surface while in (e) it is being pulled along a 45° velocity vector. For Figures 24 and 25, we have chosen to illustrate the change in tilt angle and cartoon representation for nanorods with the lowest permeation velocity providing the nanorod sufficient time for interaction between the PEG ligands and the lipid molecule head and tail groups. However, cartoon trajectories are similar to those pictured in Figure 25 for all pulling velocities we studied. We display only one example of a nanorod trajectory in Figure 25, but it is clear from Figure 24 that there are many permeation pathways accessible to the functionalised nanorod for any given initial angle. Note that in all trajectories, regardless of the initial angle of entry, the PEGylated nanorod passes through the parallel to the membrane surface configuration inside the membrane, and in all cases, leaves the membrane at close to either 0° or 180°, i.e. perpendicular to the membrane surface.

In the cartoon representations from Figure 25, we noticed a theme in the permeation pathway of a nanorod; in every instance, the nanorod undergoes a rotational motion, passing through a lying down orientation and then straightening up upon exit. To further understand the mechanism of this rotational behaviour, we produced snapshots of the permeation pathway at 30 ns intervals for PEGylated nanorods permeating at the lowest velocity (0.05 m/s). We display these snapshots for Method 1 and Method 2 in Figures 26 and 27. Although we have data for many entry angles we show only the examples where the initial tilt angle is 45° but the difference lies in the way we allow the nanorod to permeate the membrane, as described above, corresponding to the cartoons in Figure 25(c) and (e).

We observe that the PEGylated nanorod tilts further to lie parallel to the membrane as it begins the adsorption stage. This occurs immediately when the leading PEG ligands begin to interact with the lipid head groups in the first membrane leaflet. As the nanorod exits the membrane, it begins to straighten up along the membrane normal while the trailing PEG ligands continue to interact with the lipid head groups in the bottom leaflet of the membrane.

From our earlier studies with PEGylated spherical gold nanoparticles, we observed that favourable hydrophilic interactions between the PEG ligands and lipid head groups resulted in curving of the membrane in the nanoparticle adsorption stage. This is in contrast to our studies with alkanethiol-protected gold nanoparticles in which the alkanethiol ligands break the membrane leaflet to form a hole in order to interact favourably with the hydrophobic lipid tails. We therefore expect that the tilting behaviour of the nanorod occurs in order to maximise the favorable hydrophilic interactions between the lipid head molecules and PEG ligands, as well as to overcome the energetic barrier of permeation. In Figures 26 and 27 we highlight in blue the PEG beads which come within 1.0 nm of the choline and phosphate lipid head groups (the cut-off distance for the shifted LJ potential in our system is 1.2 nm). The blue patches in the snapshots thus constitute the number of favourable interactions between PEG and the lipid head groups. Thus, in Figure 26, we can visually follow the progression of attractive interactions that favour the nanorod positioning itself during the permeation process. The favourable hydrophilic interactions between the PEG beads and phosphate and choline head groups (shown by the blue patches) drives the nanorod to lie in a particular way that maximises this

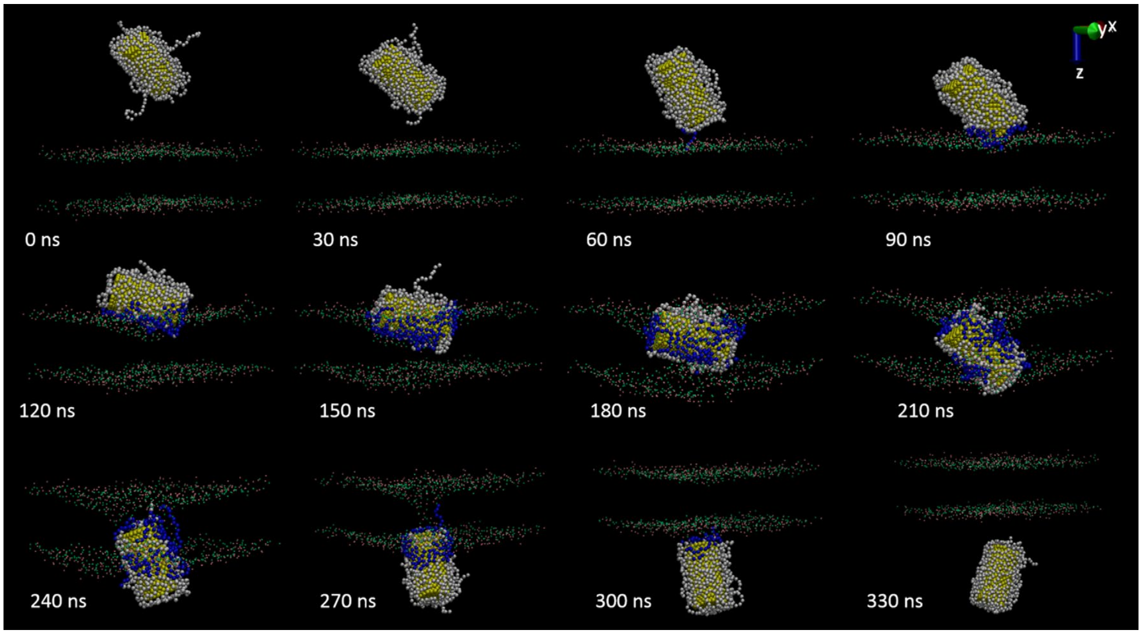

Figure 26. (Colour online) Molecular snapshots of permeation (utilising Method 1) of PEGylated gold nanorod in the lipid bilayer membrane initial angle of 45° where pink = choline, green = phosphate, yellow = AuNR core, white = PEG ligands, and blue = PEG beads within 1.0 nm of choline and phosphate molecules. The cartoon in Figure 8(c) shows this particular trajectory. Reproduced from Ref. [103].

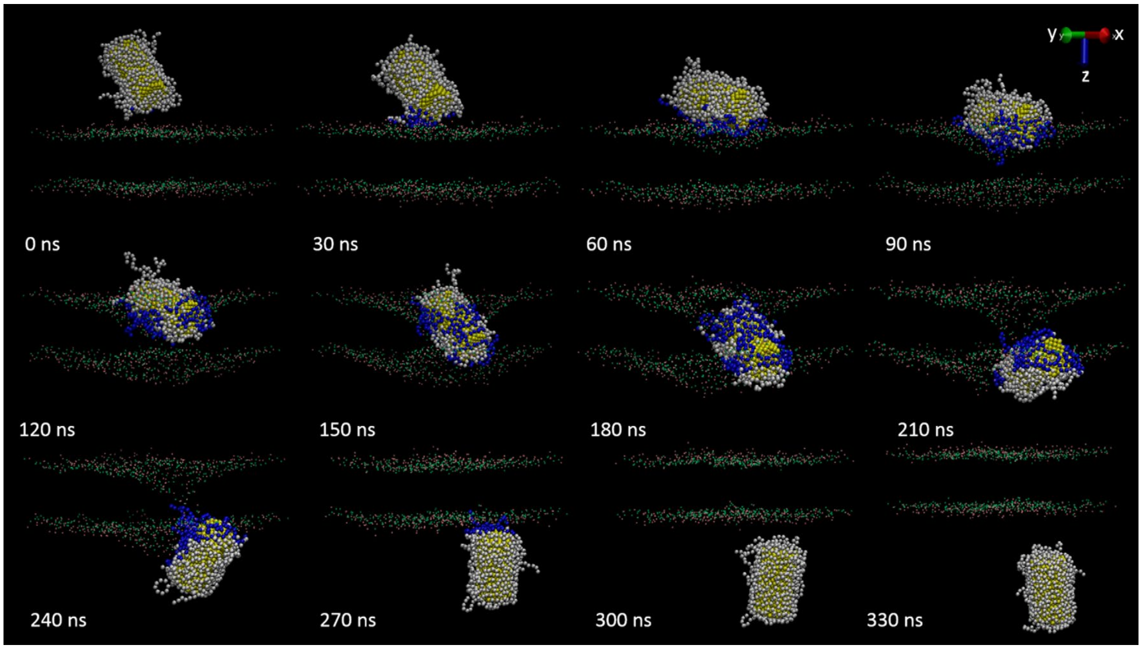

Figure 27. (Colour online) Molecular snapshots of permeation (utilising Method 2) of PEGylated gold nanorod in the lipid bilayer membrane initial angle of 45° where pink = choline, green = phosphate, yellow = AuNR core, white = PEG ligands, and blue = PEG beads within 1.0 nm of choline and phosphate molecules. The cartoon in Figure 8(c) shows this particular trajectory. Reproduced from Ref. [103].

interaction, i.e. so as to allow a large number of PEG beads to interact favourably with the lipid head groups.

In Figure 26 we see that lying down is accompanied by an increasing blue-patch area as the lying down position permits more contacts of PEG with head groups. As the nanorod proceeds through the middle region of the membrane, the PEG ligands of the nanorod reach up to the heads of the top leaflet, the PEG ligands at the bottom of the nanorod reach out to the heads of the bottom leaflet, as seen by the blue patches at both ends, whereas the PEG ligands in the torso seem to retract, presenting a slimmer projectile passing through the lipid tail regions. Keeping the trailing end in touch with the lower leaflet head groups as it exits permits the final bit of favourable interactions, and so of course exit has to be in a straightened up orientation to facilitate all these.

In Figure 27, we present snapshots of Method 2, where the nanorod was pulled by its centre-of-mass atom at a constant velocity with a velocity vector that maintained the angle at 45°

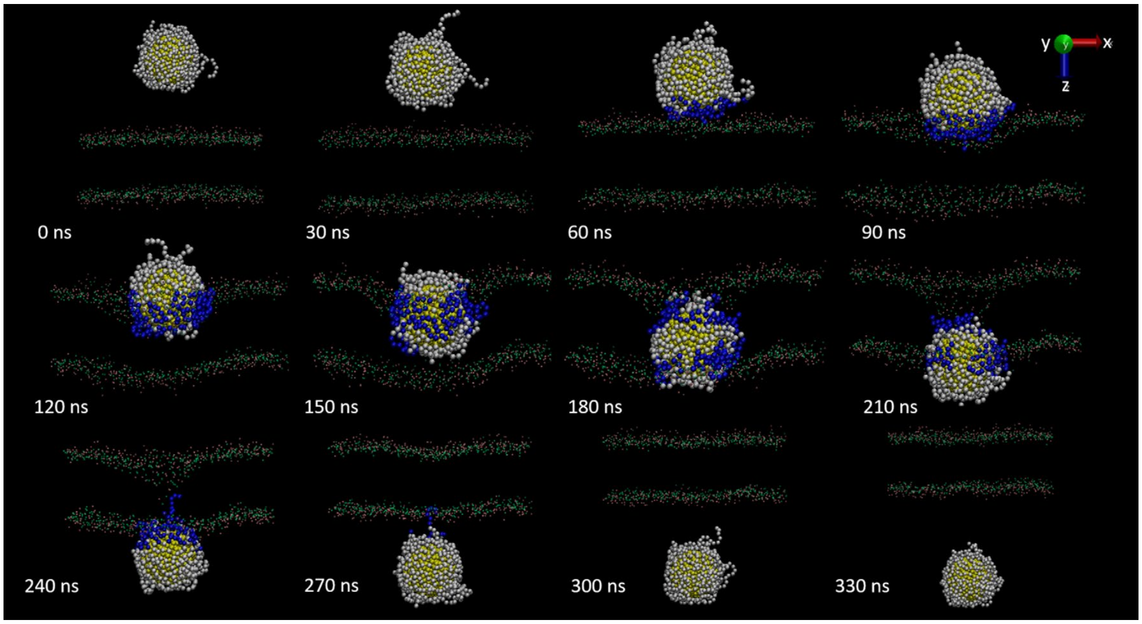

Figure 28. (Colour online) Molecular snapshots of permeation of PEGylated spherical gold nanoparticle in the lipid bilayer membrane where pink = choline, green = phosphate, yellow = AuNR core, white = PEG ligands, and blue = PEG beads within 1.0 nm of choline and phosphate molecules.

relative to the membrane normal. We see in the snapshots from Figure 27 that the nanorod lies down in the membrane surface almost immediately as the permeation process begins and the growth of the blue patches explains why. As the permeation continues, the nanorod begins to straighten up and finally exits the membrane, in a similar way as in Figure 26. There is a slight difference between the two sets of snapshots where we see that the nanorod exits the membrane more quickly in Method 2 at 210–240 ns while in Method 1, the exit occurs closer to 270–300 ns. This occurs since in Method 2, the nanorod lies down on the membrane surface immediately compared to Method 2 due to the applied velocity vector facilitating such a rotation.

For comparison, we also show the snapshots of the permeation pathway of a spherical PEGylated gold nanoparticle (Figure 28). Upon approach to the membrane (the adsorption stage), the membrane develops a curvature where the PEG ligands curl upwards toward the nanoparticle surface and interact closely with the lipid head groups; this occurs in both the nanorod (Figures 26 and 27) and spherical nanoparticle case (Figure 28). In Figure 28, we see at 210 ns that the nanoparticle has passed the first bilayer membrane leaflet and is at the position of the second membrane leaflet. In Figure 26, at 210 ns the nanorod is interacting with both the bottom and the top membrane leaflet, lying down in an orientation that maximises its favourable hydrophilic interactions with PEG ligands and lipid head groups. We see that at 240 ns, even while the nanorod is beginning to exit, it is still interacting favourably with the top membrane leaflet unlike the spherical case, where minimal interactions with the top leaflet occur at this stage.

In Figure 29, we show the interaction energy between the PEG beads and lipid head groups from both bilayer membrane leaflets. We see that this follows the snapshots we display in Figures 26 and 27 where the highest interaction energy (180 ns) coincides with the largest occurrence of the blue patches. The interaction energy decreases significantly as the nanorod straightens up to exit the membrane. This shows that the rotational behaviour of the PEGylated nanorod is driven by the attractive interactions between the PEG ligands and the lipid head groups.

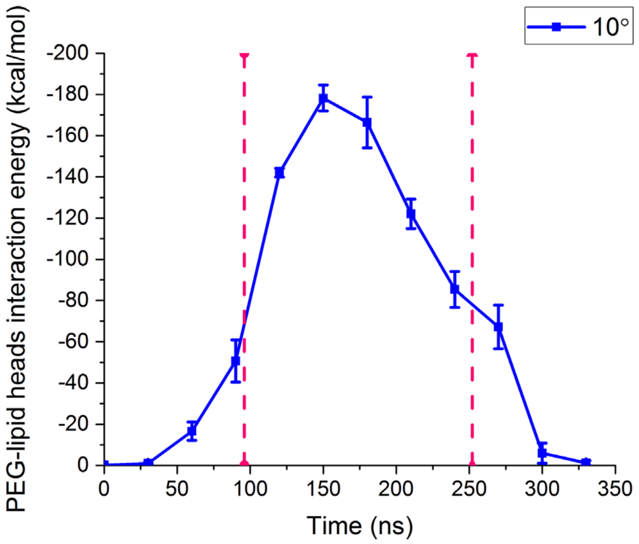

Figure 29. (Colour online) Total interaction energy between all PEG beads and phosphate and choline lipid head groups along the course of nanorod permeation under initial angle of 10° (utilising Method 1). Each data point has error bars incorporated based on three independent simulations. The pink dashed lines represent the time when the centre-of-mass of the PEGylated nanorod is 2.0 nm above from the top membrane leaflet and later, when it is 2.0 nm below the bottom membrane leaflet. Reproduced from Ref. [103].

Neither the nanorod nor the spherical nanoparticle drag lipid molecules away from the membrane (advantage of PEG, discussed earlier). In terms of a nanocarrier choice, the spherical nanoparticle causes less damage to both the top and bottom membrane leaflets compared to the gold nanorod. This is brought home more clearly by considering the water penetration profiles in Figure 30.

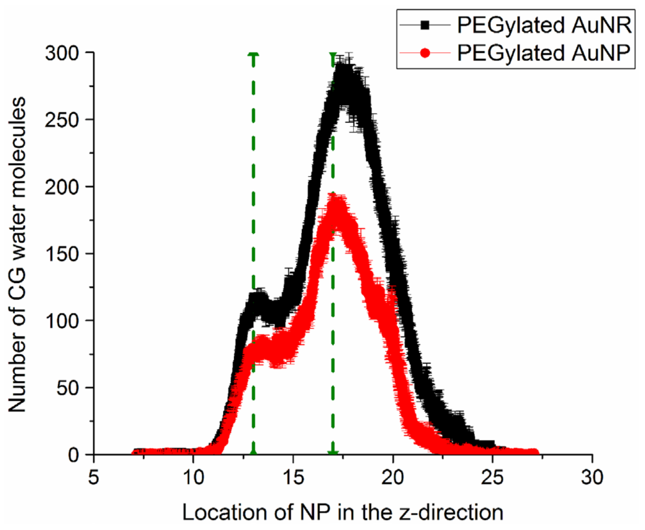

Figure 30. (Colour online) Number of coarse-grained water molecules that permeate into the hydrophobic membrane interior during permeation of PEGylated gold nanoparticles with Au cores of identical volume, illustrating the effect of aspect ratio. The green dotted lines represent the equilibrated position of the phosphate groups in the top and bottom membrane leaflet. Each data point contains error bars associated with three independent simulations.

Both the PEGylated spherical gold nanoparticle and gold nanorod have the same core volume, but the grafting density differs as mentioned previously, due to the shape of the gold core. We examine the water leakage for the PEGylated AuNR where the initial tilt angle is 90°. We see in Figure 30 that a greater number of water molecules enter the hydrophobic interior during the permeation of the PEGylated gold nanorod compared to a spherical nanoparticle. It is expected that permeation with a PEGylated gold nanorod results in higher numbers of water molecules penetrating the hydrophobic membrane interior; since the PEGylated nanorod disturbs both the top and bottom membrane leaflet while lying down, it allows more water molecules to enter the membrane interior. As shown in Figure 30, there is a slight increase in water molecule penetration before the nanorod enters the membrane; this occurs since the nanorod not only lies down on the membrane before entry, it also disturbs the lipid head groups in the top leaflet in the process of changing its orientation towards lying down. This results in water molecules entering the membrane interior even before the leading edge of the nanorod has travelled past the first membrane leaflet (indicated by the vertical dashed line in Figure 30). At the exit stage, we observe in both cases that water molecules begin to leave the membrane interior as soon as the nanoparticle passes the second membrane leaflet (indicated by the second vertical line in Figure 30). This is characteristic of PEGylated nanocarriers which cause less disturbance to the membrane overall and allow for recovery to begin immediately. We notice however that there are more water molecules within the membrane interior at this stage for the PEGylated nanorod case; this can be attributed to the turning of the nanorod upon exit, which does not occur in the spherical PEGylated nanoparticle.

During permeation of the PEGylated nanorod, we tracked the compartments into which the water molecules eventually reached and found that of the approximately 300 water molecules that entered the hydrophobic interior, around 2% of these waters did not return to their original compartment. This was consistent for all entry angles at the lower pulling velocities. For higher permeation velocities, around 6% of the water molecules did not return to their original compartment once they entered the membrane interior. Essentially, few water molecules translocated to the opposite membrane compartment during PEGylated nanorod permeation.

4. Conclusions

What distinguishes soft matter from more rigid solids is its range of dynamics, structural dependence on temperature, large number of internal (conformational) degrees of freedom and magnitudes of thermal fluctuations (entropy considerations), greater range of response to interfacial intrusion, primarily stemming from the weak interactions between structural elements, thereby resulting in a delicate balance between enthalpic and entropic contributions to the free energy. In turn this leads to sensitivity of structure and dynamics to minor changes in external conditions and minor alterations in composition. The consequences of these characteristics are that prediction of macroscopic behaviour is not as straightforward as in surfaces of rigid ionic or covalently bonded inorganic networks. Soft matter is where MD can make significant contributions to the understanding and prediction of behaviour. By following the motions of atoms or small groupings of atoms behaving under the influence of a pre-determined set of interatomic or intergroup interaction potentials, the delicate balance between the enthalpic and entropic contributions to free energy is taken into account and detailed mechanisms of sub-molecular level behaviour can be 'observed' in addition to obtaining those average quantities such as counts of events, distributions of conformations, distributions of constituents, average values of macroscopic properties, that could be compared with experimental observations. In this paper we have provided many examples of detailed sub-molecular level behaviour by exploring various parameters of the permeant, such as size, shape, bare or surface-functionalised (ligand-grafted), type of ligands, lengths of ligands, etc. We now can make the following generalisations from our examples: we have observed that functionalised nanoparticles with hydrophobic ligands potentially have negative consequences on lipid bilayer membranes after permeation is complete, the extent of which depending on size, surface coverage and ligand length. Hydrophobic nanoparticles cause lipid molecules to be displaced from the membrane due to favourable hydrophobic interactions with lipid tails. Incidences of lipid displacement increase with hydrophobic nanoparticles that have large core diameters and longer ligands; in these cases a larger pore is formed in the membrane during permeation and greater numbers of lipid molecules are displaced. Lipid flip-flop events rarely occur as a result of permeation with a hydrophobic nanoparticle since a majority of lipid molecules are carried away into the bulk solution and lose the ability to return to the leaflets. On the other hand, lack of formation of a water column as a consequence of permeation with a hydrophobic nanoparticle hinders undesirable ion transport across the membrane. Overall, we observe that full recovery of the membrane is least likely with a nanoparticle functionalised with hydrophobic ligands.

In cases where a nanoparticle is functionalised with hydrophilic ligands, membrane recovery was observed to occur immediately after the nanoparticle exited the membrane. We found that water molecules present in the membrane interior begin to leave the membrane as soon as the nanoparticle passes the second leaflet. Nanoparticles with larger core diameters, longer ligands, and higher surface coverage densities of hydrophilic ligands develop larger pores in the membrane due to a larger overall size. Nevertheless, we observed that even in cases with high surface coverage and long ligands, membrane recovery was successful for nanoparticles with hydrophilic ligands. Lipid molecules complete the flip-flop events and are not dragged into the bulk solution; unlike in the case of the hydrophobic nanoparticle. Ion penetration rarely occurs since the membrane recovery occurs immediately and water and ion molecules present in the membrane interior are expelled to the aqueous compartments. With the exception of lipid flip-flop events, we have determined that nanoparticles functionalised with hydrophilic ligands are less damaging in comparison to those protected by hydrophobic ligands and should be considered viable candidates for drug delivery applications.

We found that nanorods protected with hydrophilic ligand groups undergo rotational behaviour where, irrespective of the initial orientation of the nanorod to the membrane, a 'lying down and then straightening up upon exit' permeation pathway occurs. Similar to their spherical counterparts, they do not remove lipid molecules from the membrane leaflets and also allow for membrane recovery to occur. Larger numbers of water molecules enter the membrane as a consequence of permeation with nanorods, in comparison to spherical nanoparticles; however, they are still practical candidates for biomedical applications since the hydrophilic ligands permit permeation with little or no damage to the lipid membrane.

In conclusion, molecular dynamics simulations are an essential tool for the understanding of the molecular-level events accompanying adsorption, permeation, and possible entrapment/accumulation of small molecules at/into soft matter surfaces. Experimentalists designing nanocarriers for drug delivery can use the results from our simulations when considering development of nanoparticles protected with biocompatible hydrophilic ligand groups that can aid in the non-disruptive movement of the nanocarrier *in vivo*.

Disclosure statement

No potential conflict of interest was reported by the authors.

Funding

This work was supported by the National Science Foundation [grant number CBET-1545560/1263107].

ORCID

Sohail Murad http://orcid.org/0000-0002-1486-0680

References

[1] Zwolinski BJ, Eyring H, Reese CE. Diffusion and membrane permeability. J Phys Coll Chem. 1949;53:1426–1453.

[2] Lieb WR, Stein WD. Biological membranes behave as non-porous polymeric sheets with respect to the diffusion of non-electrolytes. Nature. 1969;224:240–243.

[3] Crank J, Park GS. Diffusion in polymers. London: Academic Press; 1968.

[4] Träuble H. The movement of molecules across lipid membranes: a molecular theory. J Membrane Biol. 1971;4:193–208.

[5] Qiao B, Olvera de la Cruz M. Driving force for water permeation across lipid membranes. J Phys Chem Lett. 2013;4(19):3233–3237.

[6] Yuan HJ, Jameson CJ, Murad S. Exploring gas permeability of lipid membranes using coarse-grained molecular dynamics. Mol Simul. 2009;35:953–961.

[7] Monticelli L, Kandasamy SK, Periole X, et al. The MARTINI coarse-grained force field: extension to proteins. J Chem Theory Comput. 2008;4:819–834.

[8] Marrink SJ, Risselada HJ, Yefimov S, et al. The MARTINI force field: coarse grained model for biomolecular simulations. J Phys Chem B. 2007;111:7812–7824.

[9] Baron R, de Vries AH, Hünenberger PH, et al. Configurational entropies of lipids in pure and mixed bilayers from atomic-level and coarse-grained molecular dynamics simulations. J Phys Chem B. 2006;110:15602–15614.

[10] Yuan HJ, Jameson CJ, Murad S. Diffusion of gases across lipid membranes with OmpA channel: a molecular dynamics study. Mol Phys. 2010;108:1569–1581.

[11] Nagle JF, Tristram-Nagle S. Structure of lipid bilayers. Biochim Biophys Acta. 2000;1469(3):159–195.

[12] Krishnamurthy M, Murad S, Olson JD. Molecular dynamics simulation of Henry's constant of argon, nitrogen, methane and oxygen in ethylene oxide. Mol Simulat. 2006;32:11–16.

[13] Bohn M, Lago S, Fischer J, et al. Excess properties of liquid mixtures from perturbation theory: results for model systems and predictions for real systems. Fluid Phase Equilibr. 1985;23:137–151.

[14] Harris JG, Yung KH. Carbon dioxide's liquid-vapor coexistence curve and critical properties as predicted by a simple molecular model. J Phys Chem. 1995;99:12021–12024.

[15] Maitland GC, Rigby M, Smith EB, et al. Intermolecular forces. Oxford: Oxford University Press; 1981.

[16] Wang Y, Cohen J, Boron WF, et al. Exploring gas permeability of cellular membranes and membrane channels with molecular dynamics. J Struct Biol. 2007;157:534–544.

[17] Marrink SJ, de Vries AH, Mark AE. Coarse grained model for semiquantitative lipid simulations. J Phys Chem B. 2004;108:750–760.

[18] Marrink SJ, Berendsen HJC. Simulation of water transport through a lipid membrane. J Phys Chem. 1994;98:4155–4168.

[19] Marrink SJ, Berendsen HJC. Permeation process of small molecules across lipid membranes studied by molecular dynamics simulations. J Phys Chem. 1996;100:16729–16738.

[20] Jansen M, Blume A. A comparative study of diffusive and osmotic water permeation across bilayers composed of phospholipids with different head groups and fatty acyl chains. Biophys J. 1995;68:997–1008.

[21] Paula S, Volkov AG, Van Hoek AN, et al. Permeation of protons, potassium ions, and small polar molecules through phospholipid bilayers as a function of membrane thickness. Biophys J. 1996;70:339–348.

[22] Murad S, Oder K, Lin J. Molecular simulation of osmosis, reverse osmosis, and electro-osmosis in aqueous and methanolic electrolyte solutions. Mol Phys. 1998;95:401–408.

[23] Oder K, Murad S. Molecular simulations of membrane based separations of supercritical electrolyte solutions. Mol Simul. 2000;25:229–238.

[24] Mang X, Zeng X, Tang B, et al. Control of anisotropic self-assembly of gold nanoparticles coated with mesogens. J Mat Chem. 2012;22(22):11101–11106.

[25] Nilges M, Clore GM, Gronenborn AM. Determination of three-dimensional structures of proteins from interproton distance data by dynamical simulated annealing from a random array of atoms circumventing problems associated with folding. FEBS Lett. 1988;239(1):129–136.

[26] Boisselier E, Astruc D. Gold nanoparticles in nanomedicine: preparations, imaging, diagnostics, therapies and toxicity. Chem Soc Rev. 2009;38(6):1759–1782.

[27] Jain PK, Huang XH, El-Sayed IH, et al. Noble metals on the nanoscale: optical and photothermal properties and some applications in imaging, sensing, biology, and medicine. Accounts Chem Res. 2008;41(12):1578–1586.

[28] Sperling RA, Rivera Gil P, Zhang F, et al. Biological applications of gold nanoparticles. Chem Soc Rev. 2008;37(9):1896–1908.

[29] Connor EE, Mwamuka J, Gole A, et al. Gold nanoparticles are taken up by human cells but do not cause acute cytotoxicity. Small. 2005;1(3):325–327.

[30] El-Sayed IH, Huang XH, El-Sayed M. Surface plasmon resonance scattering and absorption of anti-EGFR antibody conjugated gold nanoparticles in cancer diagnostics: applications in oral cancer. Nano Lett. 2005;5(5):829–834.

[31] Luedtke WD, Landman U. Structure and thermodynamics of self-assembled monolayers on gold nanocrystallites. J Phys Chem B. 1998;102(34):6566–6572.

[32] Hostetler MJ, Wingate JE, Zhong CJ, et al. Alkanethiolate gold cluster molecules with core diameters from 1.5 to 5.2 nm: core and monolayer properties as a function of core size. Langmuir. 1998;14(1):17–30.

[33] Song B, Yuan HJ, Jameson CJ, et al. Role of surface ligands in nanoparticle permeation through a model membrane: a coarse-grained molecular dynamics simulations study. Mol Phys. 2012;110:2181–2195.

[34] Tiwari PM, Vig K, Dennis VA, et al. Functionalized gold nanoparticles and their biomedical applications. Nanomaterials. 2011;1(1):31–63.

[35] Cho WS, Cho M, Jeong J, et al. Size-dependent tissue kinetics of PEG-coated gold nanoparticles. Toxicol Appl Pharmacol. 2010;245(1):116–123.

[36] Pan Y, Neuss S, Leifert A, et al. Size-dependent cytotoxicity of gold nanoparticles. Small. 2007;3(11):1941–1949.

[37] Hainfeld JF, Slatkin DN, Smilowitz HM. The use of gold nanoparticles to enhance radiotherapy in mice. Phys Med Biol. 2004;49(18):N309–N315.

[38] Lee OS, Schatz GS. Interaction between DNAs on a gold surface. J Phys Chem C. 2009;113(36):15941–15947.

[39] Lee OS, Schatz GS. Molecular dynamics simulation of DNA-functionalized gold nanoparticles. J Phys Chem C. 2009;113(6):2316–2321.

[40] Chang CI, Lee WJ, Young TF, et al. Adsorption mechanism of water molecules surrounding Au nanoparticles of different sizes. J Chem Phys. 2008;128(15):154703.

[41] Lin J, Zhang H, Chen Z, et al. Penetration of lipid membranes by gold nanoparticles: insights into cellular uptake, cytotoxicity, and their relationship. ACS Nano. 2010;4(9):5421–5429.

[42] Höfler L, Gyurcsányi RE. Coarse grained molecular dynamics simulation of electromechanically-gated DNA modified conical nanopores. Electroanalysis. 2008;20(3):301–307.

[43] Chevigny C, Dalmas F, Di Cola E, et al. Polymer-grafted-nanoparticles nanocomposites: dispersion, grafted chain conformation, and rheological behavior. Macromolecules. 2010;44(1):122–133.

[44] Wu C. Simulated glass transition of poly (ethylene oxide) bulk and film: a comparative study. J Phys Chem B. 2001;115(38):11044–11052.

[45] Barbier D, Brown D, Grillet AC, et al. Interface between end-functionalized PEO oligomers and a silica nanoparticle studied by molecular dynamics simulations. Macromolecules. 2004;37(12):4695–4710.

[46] Ghanbari A, Rahimi M, Dehghany J. Influence of surface grafted polymers on the polymer dynamics in a silica-polystyrene nanocomposite: A coarse-grained molecular dynamics investigation. J Phys Chem C. 2013;117(47):25069–25076.

[47] Corbierre MK, Cameron NS, Sutton M, et al. Polymer-stabilized gold nanoparticles and their incorporation into polymer matrices. J Am Chem Soc. 2001;123(42):10411–10412.

[48] Smith JS, Bedrov D., Smith GD. A molecular dynamics simulation study of nanoparticle interactions in a model polymer-nanoparticle composite. Compos Sci Technol. 2003;63(11):1599–1605.

[49] Ndoro TV, Voyiatzis E, Ghanbari A, et al. Interface of grafted and ungrafted silica nanoparticles with a polystyrene matrix: atomistic molecular dynamics simulations. Macromolecules. 2011;44(7):2316–2327.

[50] Hong B, Panagiotopoulos AZ. Molecular dynamics simulations of silica nanoparticles grafted with Poly(ethylene oxide) oligomer chains. J Phys Chem B. 2012;116(8):2385–2395.

[51] Karakoti AS, Das S, Thevuthasan S, et al. PEGylated inorganic nanoparticles. Angew Chem Int Ed Engl. 2011;50(9):1980–1994.

[52] Manson J, Kumar D, Meenan BJ, et al. Polyethylene glycol functionalized gold nanoparticles: the influence of capping density on stability in various media. Gold Bull. 2011;44(2):99–105.

[53] Song B, Yuan H, Jameson CJ, et al. Permeation of nanocrystals across lipid membranes. Mol Phys. 2011;109:1511–1526.

[54] Zeng Q, Yu A, Lu G. Evaluation of interaction forces between nanoparticles by molecular dynamics simulation. Ind Eng Chem Res. 2010;49:12793–12797.

[55] Vasir JK, Labhasetwar V. Quantification of the force of nanoparticle-cell membrane interactions and its influence on intracellular trafficking of nanoparticles. Biomaterials. 2008;29:4244–4252.

[56] Lee OS, Schatz GC. Computational simulations of the interaction of lipid membranes with DNA-functionalized gold nanoparticles. Methods Mol Biol. 2011;726:283–296.

[57] Wallace EJ, Sansom MSP. Blocking of carbon nanotube based nanoinjectors by lipids: a simulation study. Nano Lett. 2008;8:2751–2756.

[58] Plimpton S. Fast parallel algorithms for short-range molecular dynamics. J Comput Phys. 1995;117(1):1–19.

[59] Marrink SJ, Risselada HJ, Yefimov S, et al. The MARTINI force field: coarse grained model for biomolecular simulations. J Phys Chem B. 2007;111:7812–7824.

[60] Matysiak S, Clementi C, Praprotnik M, et al. Modeling diffusive dynamics in adaptive resolution simulation of liquid water. J Chem Phys. 2008;128:024503.

[61] Subczynski WK, Hopwood LE, Hyde JS. Is the mammalian cell plasma membrane a barrier to oxygen transport? J Gen Physiol. 1992;100:69–87.

[62] Lin JQ, Zhang HW, Chen Z, et al. Penetration of lipid membranes by gold nanoparticles: Insights into cellular uptake, cytotoxicity, and their relationship. ACS Nano. 2010;4(9):5421–5429.

[63] Wang B, Zhang L, Bae SC, et al. Nanoparticle-induced surface reconstruction of phospholipid membranes. Proc Natl Acad Sci USA. 2008;105:18171–18175.

[64] Oroskar PA, Jameson CJ, Murad S. Simulated permeation and characterization of PEGylated gold nanoparticles in a lipid bilayer system. Langmuir. 2016;32:7541–7555.

[65] Manson J, Kumar D, Meenan BJ, et al. Polyethylene glycol functionalized gold nanoparticles: the influence of capping density on stability in various media. Gold Bull. 2011;44(2):99–105.

[66] Rahme K, Chen L, Hobbs RG, et al. PEGylated gold nanoparticles: polymer quantification as a function of PEG lengths and nanoparticle dimensions. RSC Adv. 2013;3(17):6085–6094.

[67] Nicholas AR, Scott MJ, Kennedy NI, et al. Effect of grafted polyethylene glycol (PEG) on the size, encapsulation efficiency and permeability of vesicles. BBA-Biomemb. 2000;1463(1):167–178.

[68] Tirosh O, Barenholz Y, Katzhendler J, et al. Hydration of polyethylene glycol-grafted liposomes. Biophys J. 1998;74(3):1371–1379.

[69] Hattemer GD, Arya G. Viscoelastic properties of polymer-grafted nanoparticle composites from molecular dynamics simulations. Macromolecules. 2015;48(4):1240–1255.

[70] Frischknecht AL. Forces between nanorods with end-adsorbed chains in a homopolymer melt. J Chem Phys. 2008;128(22):224902.

[71] Anne A, Demaille C, Moiroux J. Terminal attachment of polyethylene glycol (PEG) chains to a gold electrode surface. Cyclic voltammetry applied to the quantitative characterization of the flexibility of the attached PEG chains and of their penetration by mobile PEG chains. Macromolecules. 2002;35(14):5578–5586.

[72] Rissanen S, Kumorek M, Martinez-Seara H, et al. Effect of PEGylation on drug entry into lipid bilayer. J Phys Chem B. 2013;118(1):144–151.

[73] Magarkar A, Karakas E, Stepniewski M, et al. Molecular dynamics simulation of PEGylated bilayer interacting with salt ions: a model of the liposome surface in the bloodstream. J Phys Chem B. 2012;116(14):4212–4219.

[74] Stepniewski M, Pasenkiewicz-Gierula M, Róg T, et al. Study of PEGylated lipid layers as a model for PEGylated liposome surfaces: molecular dynamics simulation and langmuir monolayer studies. Langmuir. 2011;27(12):7788–7798.

[75] Li YC, Rissanen S, Stepniewski M, et al. Study of interaction between PEG carrier and three relevant drug molecules: piroxicam, paclitaxel, and hematoporphyrin. J Phys Chem B. 2012;116(24):7334–7341.

[76] Panyam J, Labhasetwar V. Biodegradable nanoparticles for drug and gene delivery to cells and tissue. Adv Drug Deliv Rev. 2003;55(3):329–347.

[77] Kumari A, Yadav SK, Yadav SC. Biodegradable polymeric nanoparticles based drug delivery systems. Colloids Surf B. 2010;75(1):1–18.

[78] Yoo HS, Lee KH, Oh JE, et al. In vitro and *in vivo* anti-tumor activities of nanoparticles based on doxorubicin–PLGA conjugates. J Control Release. 2000;68(3):419–431.

[79] Yoo JW, Chambers E, Mitragotri S. Factors that control the circulation time of nanoparticles in blood: challenges, solutions and future prospects. Curr Pharm Des. 2010;16(21):2298–2307.

[80] He Z, Liu J, Du L. The unexpected effect of PEGylated gold nanoparticles on the primary function of erythrocytes. Nanoscale. 2014;6(15):9017–9024.

[81] Song B, Yuan H, Pham SV, et al. Nanoparticle permeation induces water penetration, ion transport, and lipid flip-flop. Langmuir. 2012;28(49):16989–17000.

[82] Oroskar PA, Jameson CJ, Murad S. Surface-functionalized nanoparticle permeation triggers lipid displacement and water and ion leakage. Langmuir. 2015;31(3):1074–1085.

[83] Lu W, Sun Q, Wan J, et al. Cationic albumin-conjugated pegylated nanoparticles allow gene delivery into brain tumors via intravenous administration. Cancer Res. 2006;66(24):11878–11887.

[84] Kim HR, Gil S, Andrieux K, et al. Low-density lipoprotein receptor-mediated endocytosis of PEGylated nanoparticles in rat brain endothelial cells. Cell Mol Life Sci. 2007;64(3):356–364.

[85] Bennett WD, Tieleman DP. Water defect and pore formation in atomistic and coarse-grained lipid membranes: pushing the limits of coarse graining. J Chem Theory Comput. 2011;7(9):2981–2988.

[86] Tieleman DP, Marrink SJ. Lipids out of equilibrium: energetics of desorption and pore mediated flip-flop. J Amer Chem Soc. 2006;128(38):12462–12467.

[87] Lodish H, Berk A, Zipursky SL, et al. Molecular cell biology. 4th ed. New York (NY): W.H. Freeman; 2000.

[88] Khavrutskii IV, Gorfe AA, Lu B, et al. Free energy for the permeation of Na + and Cl − ions and their ion-pair through a zwitterionic dimyristoyl phosphatidylcholine lipid bilayer by umbrella integration with harmonic Fourier beads. J Amer Chem Soc. 2009;131(5):1706–1716.

[89] Wilson MA, Pohorille A. Mechanism of unassisted ion transport across membrane bilayers. J Amer Chem Soc. 1996;118(28):6580–6587.

[90] Schweighofer KJ, Benjamin I. Electric field effects on the structure and dynamics at a liquid–liquid interface. J Electro Anal Chem. 1995;391(1–2):1–10.

[91] Luo G, Malkova S, Yoon J, et al. Ion distributions near a liquid-liquid interface. Science. 2006;311(5758):216–218.

[92] Benjamin I. Dynamics of ion transfer across a liquid–liquid interface: a comparison between molecular dynamics and a diffusion model. J Chem Phys. 1992;96(1):577–585.

[93] Yamashita T, Voth GA. Properties of hydrated excess protons near phospholipid bilayers. J Phys Chem B. 2009;114(1):592–603.

[94] Daleke DL. Phospholipid flippases. J Biol Chem. 2007;282(2):821–825.

[95] Matsuzaki K, Murase O, Fujii N, et al. An antimicrobial peptide, magainin 2, induced rapid flip-flop of phospholipids coupled with pore formation and peptide translocation. Biochemistry. 1996;35(35):11361–11368.

[96] Devaux PF. Static and dynamic lipid asymmetry in cell membranes. Biochemistry. 1991;30(5):1163–1173.

[97] Wallace EJ, Sansom MS. Blocking of carbon nanotube based nanoinjectors by lipids: a simulation study. Nano Lett. 2008;8(9):2751–2756.

[98] Albanese A, Tang PS, Chan WC. The effect of nanoparticle size, shape, and surface chemistry on biological systems. Annu Rev Biomed Eng. 2012;14:1–16.

[99] Li Y, Kröger M, Liu WK. Shape effect in cellular uptake of PEGylated nanoparticles: comparison between sphere, rod, cube and disk. Nanoscale. 2015;7(40):16631–16646.

[100] Loverde SM, Klein ML, Discher DE. Nanoparticle shape improves delivery: rational coarse grain molecular dynamics (rCG-MD) of taxol in worm-like PEG-PCL micelles. Adv Mater. 2012;24(28):3823–3830.

[101] Huang X, Jain PK, El-Sayed IH, et al. Plasmonic photothermal therapy (PPTT) using gold nanoparticles. Laser Med Sci. 2008;23(3):217–228.

[102] Huff TB, Tong L, Zhao Y, et al. Hyperthermic effects of gold nanorods on tumor cells. Future Med. 2007;2(1):125–132.

[103] Oroskar PA, Jameson CJ, Murad S. Rotational behavior of PEGylated gold nanorods in a lipid bilayer system. 1–22. doi:http://dx.doi.org/10.1080/00268976.2016.1248515.

[104] Xia X, Yang M, Wang Y, et al. Quantifying the coverage density of poly(ethylene glycol) chains on surfaces of gold nanostructures. ACS Nano. 2011;6(1):512–522.

[105] Kinnear C, Dietsch H, Clift MJ, et al. Gold nanorods: controlling their surface chemistry and complete detoxification by a two-step place exchange. Angew Chem Int Ed Engl. 2013;52(7):1934–1938.

[106] Gratton SE, Ropp PA, Pohlhaus PD, et al. The effect of particle design on cellular internalization pathways. Proc Natl Acad Sci. 2008;105(33):11613–11618.